CHALMERS
UNIVERSITY OF TECHNOLOGY

JCMT BISTRO Observations: Magnetic Field Morphology of Bubbles Associated with NGC 6334

Downloaded from: https://research.chalmers.se, 2024-10-12 08:49 UTC

Citation for the original published paper (version of record):
Tahani, M., Bastien, P., Furuya, R. et al (2023). JCMT BISTRO Observations: Magnetic Field Morphology of Bubbles Associated with NGC 6334. Astrophysical Journal, 944(2). http://dx.doi.org/10.3847/1538-4357/acac81

N.B. When citing this work, cite the original published paper.

research.chalmers.se offers the possibility of retrieving research publications produced at Chalmers University of Technology. It covers all kind of research output: articles, dissertations, conference papers, reports etc. since 2004. research.chalmers.se is administrated and maintained by Chalmers Library

(article starts on next page)

The Astrophysical Journal, 944:139 (21pp), 2023 February 20 https://doi.org/10.3847/1538-4357/acac81
© 2023. The Author(s). Published by the American Astronomical Society.
OPEN ACCESS

JCMT BISTRO Observations: Magnetic Field Morphology of Bubbles Associated with NGC 6334

Mehrnoosh Tahani[1,2], Pierre Bastien[3,4], Ray S. Furuya[5], Kate Pattle[6], Doug Johnstone[7,8], Doris Arzoumanian[9], Yasuo Doi[10], Tetsuo Hasegawa[9], Shu-ichiro Inutsuka[11], Simon Coudé[12,13], Laura Fissel[14], Michael Chun-Yuan Chen[7], Frédérick Poidevin[15,16], Sarah Sadavoy[17], Rachel Friesen[18], Patrick M. Koch[19], James Di Francesco[7,8], Gerald H. Moriarty-Schieven[8], Zhiwei Chen[20], Eun Jung Chung[21], Chakali Eswaraiah[22], Lapo Fanciullo[19,23], Tim Gledhill[24], Valentin J. M. Le Gouellec[12], Thiem Hoang[25,26], Jihye Hwang[25,26], Ji-hyun Kang[25], Kyoung Hee Kim[27,28], Florian Kirchschlager[6], Woojin Kwon[29,30], Chang Won Lee[25,26], Hong-Li Liu[31,32], Takashi Onaka[33,34], Mark G. Rawlings[35,36], Archana Soam[12,25], Motohide Tamura[33,37], Xindi Tang[38], Kohji Tomisaka[39,40], Anthony P. Whitworth[41], Jungmi Kwon[33], Thuong D. Hoang[42], Matt Redman[43], David Berry[36], Tao-Chung Ching[44,45], Jia-Wei Wang[19], Shih-Ping Lai[19,46], Keping Qiu[47,48], Derek Ward-Thompson[49], Martin Houde[50], Do-Young Byun[25,26], Huei-Ru Vivien Chen[19,46], Wen Ping Chen[51], Jungyeon Cho[21], Minho Choi[25], Yunhee Choi[25], Antonio Chrysostomou[52], Pham Ngoc Diep[53], Hao-Yuan Duan[46], Jason Fiege[54], Erica Franzmann[54], Per Friberg[36], Gary Fuller[55], Sarah F. Graves[36], Jane S. Greaves[41], Matt J. Griffin[41], Qilao Gu[31], Ilseung Han[25,26], Jennifer Hatchell[56], Saeko S. Hayashi[57], Charles L. H. Hull[58,59,60], Tsuyoshi Inoue[11], Kazunari Iwasaki[61], Il-Gyo Jeong[25], Yoshihiro Kanamori[10], Miju Kang[25], Sung-ju Kang[25], Akimasa Kataoka[39], Koji S. Kawabata[62,63,64], Francisca Kemper[65,66,67], Gwanjeong Kim[68], Jongsoo Kim[25,26], Kee-Tae Kim[25,26], Mi-Ryang Kim[25], Shinyoung Kim[25,26], Jason M. Kirk[49], Masato I. N. Kobayashi[69], Vera Konyves[49], Takayoshi Kusune[39], Kevin Lacaille[70,71], Chi-Yan Law[31,72], Chin-Fei Lee[19], Hyeseung Lee[21], Jeong-Eun Lee[73], Sang-Sung Lee[25,26], Yong-Hee Lee[36,73], Dalei Li[74], Di Li[44,75], Hua-bai Li[31], Junhao Liu[47,48], Sheng-Yuan Liu[19], Tie Liu[76], Ilse de Looze[77], A-Ran Lyo[25], Steve Mairs[36], Masafumi Matsumura[78], Brenda C. Matthews[7,8], Tetsuya Nagata[79], Fumitaka Nakamura[39,40], Hiroyuki Nakanishi[80], Nagayoshi Ohashi[19], Geumsook Park[25], Harriet Parsons[36], Nicolas Peretto[41], Tae-Soo Pyo[40,57], Lei Qian[44], Ramprasad Rao[19], Brendan Retter[41], John Richer[81,82], Andrew Rigby[41], Hiro Saito[83], Giorgio Savini[77], Anna M. M. Scaife[55], Masumichi Seta[84], Yoshito Shimajiri[9,80], Hiroko Shinnaga[80], Ya-Wen Tang[19], Yusuke Tsukamoto[80], Serena Viti[77], Hongchi Wang[85], Hsi-Wei Yen[19], Hyunju Yoo[25], Jinghua Yuan[45], Hyeong-Sik Yun[73], Tetsuya Zenko[79], Chuan-Peng Zhang[44,45], Guoyin Zhang[44], Yapeng Zhang[31], Jianjun Zhou[74], Lei Zhu[44], Philippe André[86], C. Darren Dowell[87], Stewart P. S. Eyres[49], Sam Falle[88], Sven van Loo[89], and Jean-François Robitaille[90]

[1] Banting and KIPAC Fellowships: Kavli Institute for Particle Astrophysics & Cosmology (KIPAC), Stanford University, Stanford, CA 94305, USA
mtahani@stanford.edu
[2] Dominion Radio Astrophysical Observatory, Herzberg Astronomy and Astrophysics Research Centre, National Research Council Canada, P.O. Box 248, Penticton, BC V2A 6J9 Canada
[3] Institut de Recherche sur les Exoplanètes (iREx), Université de Montréal, Département de Physique, 1375, Avenue Thérèse-Lavoie-Roux, Montréal, QC, H2V 0B3, Canada
[4] Centre de Recherche en Astrophysique du Québec (CRAQ), Université de Montréal, Département de Physique, 1375, Avenue Thérèse-Lavoie-Roux, Montréal, QC, H2V 0B3, Canada
[5] Institute of Liberal Arts and Sciences, Tokushima University, Minami Jousanajima-machi 1-1, Tokushima 770-8502, Japan
[6] Department of Physics and Astronomy, University College London, Gower Street, WC1E 6BT London, UK
[7] Department of Physics and Astronomy, University of Victoria, Victoria, BC V8P 1A1, Canada
[8] Herzberg Astronomy and Astrophysics Research Centre, National Research Council of Canada, 5071 West Saanich Road, Victoria, BC V9E 2E7, Canada
[9] National Astronomical Observatory of Japan, National Institutes of Natural Sciences, Osawa, Mitaka, Tokyo 181-8588, Japan
[10] Department of Earth Science and Astronomy, Graduate School of Arts and Sciences, The University of Tokyo, 3-8-1 Komaba, Meguro, Tokyo 153-8902, Japan
[11] Department of Physics, Graduate School of Science, Nagoya University, Furo-cho, Chikusa-ku, Nagoya 464-8602, Japan
[12] Department of Earth, Environment, and Physics, Worcester State University, Worcester, MA 01602, USA
[13] Center for Astrophysics, Harvard & Smithsonian, 60 Garden Street, Cambridge, MA 02138, USA
[14] Department of Physics, Engineering Physics and Astronomy, Queen's University, Kingston, ON K7L 3N6, Canada
[15] Instituto de Astrofisíca de Canarias, E-38200 La Laguna,Tenerife, Canary Islands, Spain
[16] Departamento de Astrofísica, Universidad de La Laguna (ULL), E-38206 La Laguna, Tenerife, Spain
[17] Department for Physics, Engineering Physics and Astrophysics, Queen's University, Kingston, ON K7L 3N6, Canada
[18] National Radio Astronomy Observatory, 520 Edgemont Road, Charlottesville, VA, 22903, USA
[19] Institute of Astronomy and Astrophysics, Academia Sinica, 11F of Astronomy-Mathematics Building, AS/NTU, No. 1, Sec. 4, Roosevelt Road, Taipei 10617, Taiwan
[20] 18 Purple Mountain Observatory, Chinese Academy of Sciences, 10 Yuanhua Road, 210023 Nanjing, People's Republic of China
[21] Department of Astronomy and Space Science, Chungnam National University, 99 Daehak-ro, Yuseong-gu, Daejeon 34134, Republic of Korea
[22] Indian Institute of Science Education and Research (IISER) Tirupati, Rami Reddy Nagar, Karakambadi Road, Mangalam (PO), Tirupati 517 507, India
[23] National Chung Hsing University, 145 Xingda Road, South Dist., Taichung City 402, Taiwan
[24] School of Physics, Astronomy & Mathematics, University of Hertfordshire, College Lane, Hatfield, Hertfordshire AL10 9AB, UK
[25] Korea Astronomy and Space Science Institute (KASI), 776 Daedeokdae-ro, Yuseong-gu, Daejeon 34055, Republic 0f Korea
[26] University of Science and Technology, Korea, 217 Gajang-ro, Yuseong-gu, Daejeon 34113, Republic of Korea
[27] Korea Astronomy and Space Science Institute, 776 Daedeokdae-ro, Yuseong-gu, Daejeon 34055, Republic of Korea
[28] Basic science building 108, 50 UNIST-gil, Eonyang-eup, Ulju-gun, Ulsan 44919, Republic of Korea
[29] Department of Earth Science Education, Seoul National University, 1 Gwanak-ro, Gwanak-gu, Seoul 08826, Republic of Korea
[30] SNU Astronomy Research Center, Seoul National University, 1 Gwanak-ro, Gwanak-gu, Seoul 08826, Republic of Korea

[31] Department of Physics, The Chinese University of Hong Kong, Shatin, N.T., People's Republic of China
[32] Departamento de Astronomía, Universidad de Concepción, Av. Esteban Iturra s/n, Distrito Universitario, 160-C, Chile
[33] Department of Astronomy, Graduate School of Science, The University of Tokyo, 7-3-1 Hongo, Bunkyo-ku, Tokyo 113-0033, Japan
[34] Department of Physics, Faculty of Science and Engineering, Meisei University, 2-1-1 Hodokubo, Hino, Tokyo 191-8506, Japan
[35] Gemini Observatory/NSF's NOIRLab, 670 N. A'ohōkū Place, Hilo, HI 96720, USA
[36] East Asian Observatory, 660 N. A'ohōkū Place, University Park, Hilo, HI 96720, USA
[37] Astrobiology Center, National Institutes of Natural Sciences, Osawa, Mitaka, Tokyo 181-8588, Japan
[38] Xinjiang Astronomical Observatory, Chinese Academy of Sciences, 830011 Urumqi, People's Republic of China
[39] Division of Theoretical Astronomy, National Astronomical Observatory of Japan, Mitaka, Tokyo 181-8588, Japan
[40] SOKENDAI (The Graduate University for Advanced Studies), Hayama, Kanagawa 240-0193, Japan
[41] School of Physics and Astronomy, Cardiff University, The Parade, Cardiff, CF24 3AA, UK
[42] Kavli Institute for the Physics and Mathematics of the Universe (Kavli IPMU, WPI), UTIAS, The University of Tokyo, Kashiwa, Chiba 277-8583, Japan
[43] Centre for Astronomy, School of Physics, National University of Ireland Galway, Galway H91 TK33, Ireland
[44] CAS Key Laboratory of FAST, National Astronomical Observatories, Chinese Academy of Sciences, People's Republic of China
[45] National Astronomical Observatories, Chinese Academy of Sciences, A20 Datun Road, Chaoyang District, Beijing 100012, People's Republic of China
[46] Institute of Astronomy and Department of Physics, National Tsing Hua University, Hsinchu 30013, Taiwan
[47] School of Astronomy and Space Science, Nanjing University, 163 Xianlin Avenue, Nanjing 210023, People's Republic of China
[48] Key Laboratory of Modern Astronomy and Astrophysics (Nanjing University), Ministry of Education, Nanjing 210023, People's Republic of China
[49] Jeremiah Horrocks Institute, University of Central Lancashire, Preston PR1 2HE, UK
[50] Department of Physics and Astronomy, The University of Western Ontario, 1151 Richmond Street, London, ON N6A 3K7, Canada
[51] Institute of Astronomy, National Central University, Chung-Li 32054, Taiwan
[52] SKA Observatory, Jodrell Bank, Lower Withington, Macclesfield SK11 9FT, UK
[53] Vietnam National Space Center, Vietnam Academy of Science and Technology, 18 Hoang Quoc Viet, Hanoi, Vietnam
[54] Department of Physics and Astronomy, The University of Manitoba, Winnipeg, MB R3T 2N2, Canada
[55] Jodrell Bank Centre for Astrophysics, School of Physics and Astronomy, University of Manchester, Oxford Road, Manchester, M13 9PL, UK
[56] Physics and Astronomy, University of Exeter, Stocker Road, Exeter, EX4 4QL, UK
[57] Subaru Telescope, National Astronomical Observatory of Japan, 650 N. A'ohōkū Place, Hilo, HI 96720, USA
[58] National Astronomical Observatory of Japan, Alonso de Córdova 3788, Office 61B, 7630422, Vitacura, Santiago, Chile
[59] Joint ALMA Observatory, Alonso de Córdova 3107, Vitacura, Santiago, Chile
[60] NAOJ Fellow
[61] Department of Environmental Systems Science, Doshisha University, Tatara, Miyakodani 1-3, Kyotanabe, Kyoto 610-0394, Japan
[62] Hiroshima Astrophysical Science Center, Hiroshima University, Kagamiyama 1-3-1, Higashi-Hiroshima, Hiroshima 739-8526, Japan
[63] Department of Physics, Hiroshima University, Kagamiyama 1-3-1, Higashi-Hiroshima, Hiroshima 739-8526, Japan
[64] Core Research for Energetic Universe (CORE-U), Hiroshima University, Kagamiyama 1-3-1, Higashi-Hiroshima, Hiroshima 739-8526, Japan
[65] Institut de Ciencies de l'Espai (ICE, CSIC), Can Magrans, s/n, E-08193 Bellaterra, Barcelona, Spain
[66] ICREA, Pg. Lluís Companys 23, Barcelona, Spain
[67] Institut d'Estudis Espacials de Catalunya (IEEC), E-08034 Barcelona, Spain
[68] Nobeyama Radio Observatory, National Astronomical Observatory of Japan, National Institutes of Natural Sciences, Nobeyama, Minamimaki, Minamisaku, Nagano 384-1305, Japan
[69] Department of Earth and Space Science, Graduate School of Science, Osaka University, 1-1 Machikaneyama-cho, Toyonaka, Osaka, Japan
[70] Department of Physics and Astronomy, McMaster University, Hamilton, ON L8S 4M1, Canada
[71] Department of Physics and Atmospheric Science, Dalhousie University, Halifax, NS B3H 4R2, Canada
[72] Department of Space, Earth & Environment, Chalmers University of Technology, SE-412 96 Gothenburg, Sweden
[73] School of Space Research, Kyung Hee University, 1732 Deogyeong-daero, Giheung-gu, Yongin-si, Gyeonggi-do 17104, Republic of Korea
[74] Xinjiang Astronomical Observatory, Chinese Academy of Sciences, 150 Science 1-Street, Urumqi 830011, Xinjiang, People's Republic of China
[75] University of Chinese Academy of Sciences, Beijing 100049, People's Republic of China
[76] Shanghai Astronomical Observatory, Chinese Academy of Sciences, 80 Nandan Road, Shanghai 200030, People's Republic of China
[77] Physics & Astronomy Dept., University College London, WC1E 6BT London, UK
[78] Faculty of Education, Kagawa University, Saiwai-cho 1-1, Takamatsu, Kagawa, 760-8522, Japan
[79] Department of Astronomy, Graduate School of Science, Kyoto University, Sakyo-ku, Kyoto 606-8502, Japan
[80] Department of Physics and Astronomy, Graduate School of Science and Engineering, Kagoshima University, 1-21-35 Korimoto, Kagoshima, Kagoshima 890-0065, Japan
[81] Astrophysics Group, Cavendish Laboratory, J J Thomson Avenue, Cambridge CB3 0HE, UK
[82] Kavli Institute for Cosmology, Institute of Astronomy, University of Cambridge, Madingley Road, Cambridge, CB3 0HA, UK
[83] Department of Astronomy and Earth Sciences, Tokyo Gakugei University, Koganei, Tokyo 184-8501, Japan
[84] Department of Physics, School of Science and Technology, Kwansei Gakuin University, 2-1 Gakuen, Sanda, Hyogo 669-1337, Japan
[85] Purple Mountain Observatory, Chinese Academy of Sciences, 2 West Beijing Road, 210008 Nanjing, People's Republic of China
[86] Laboratoire AIM CEA/DSM-CNRS-Université Paris Diderot, IRFU/Service d'Astrophysique, CEA Saclay, F-91191 Gif-sur-Yvette, France
[87] Jet Propulsion Laboratory, M/S 169-506, 4800 Oak Grove Drive, Pasadena, CA 91109, USA
[88] Department of Applied Mathematics, University of Leeds, Woodhouse Lane, Leeds LS2 9JT, UK
[89] School of Physics and Astronomy, University of Leeds, Woodhouse Lane, Leeds LS2 9JT, UK
[90] Université Grenoble Alpes, CNRS, IPAG, F-38000 Grenoble, France

Received 2022 May 1; revised 2022 December 5; accepted 2022 December 16; published 2023 February 21

Abstract

We study the HII regions associated with the NGC 6334 molecular cloud observed in the submillimeter and taken as part of the *B*-fields In STar-forming Region Observations Survey. In particular, we investigate the polarization patterns and magnetic field morphologies associated with these HII regions. Through polarization pattern and pressure calculation analyses, several of these bubbles indicate that the gas and magnetic field lines have been

Original content from this work may be used under the terms of the Creative Commons Attribution 4.0 licence. Any further distribution of this work must maintain attribution to the author(s) and the title of the work, journal citation and DOI.

pushed away from the bubble, toward an almost tangential (to the bubble) magnetic field morphology. In the densest part of NGC 6334, where the magnetic field morphology is similar to an hourglass, the polarization observations do not exhibit observable impact from HII regions. We detect two nested radial polarization patterns in a bubble to the south of NGC 6334 that correspond to the previously observed bipolar structure in this bubble. Finally, using the results of this study, we present steps (incorporating computer vision; circular Hough transform) that can be used in future studies to identify bubbles that have physically impacted magnetic field lines.

Unified Astronomy Thesaurus concepts: H II regions (694); Interstellar magnetic fields (845); Star formation (1569); Molecular clouds (1072); Dust continuum emission (412)

1. Introduction

Ionized atomic hydrogen (HII) regions around massive stars are evidence of recent star formation activity. Expansion of these HII regions and their interactions with molecular clouds (Tremblin et al. 2012) can also lead to increased density (Thompson et al. 2012; Inutsuka et al. 2015) along their edges and the initiation of a new star formation sequence (e.g., Elmegreen 1998; Deharveng et al. 2005; Zavagno et al. 2010a, 2010b; Chen et al. 2022). Conversely, stellar outflows combined with magnetic fields can reduce the efficiency of massive star formation significantly (Nakamura & Li 2007; Wang et al. 2010; Koch et al. 2012a, 2012b; Federrath 2015; Krumholz & Federrath 2019; Chen et al. 2022). In magnetohydrodynamic simulations, for instance, magnetic fields enable outflows to travel farther than distances in hydrodynamic simulations, resulting in turbulent motions and decreased star formation efficiency at greater distances (e.g., Offner & Liu 2018; Krumholz & Federrath 2019). The initial morphology of the magnetic field in the cloud relative to the HII regions also influences the star formation efficiency (Chen et al. 2022). Before examining the star formation activities caused by HII regions, it is necessary to study the magnetic field morphology of these regions and the influence of HII regions on the magnetic fields of the parent molecular cloud.

The physical sizes of HII regions range from ultracompact (<0.1 pc) to evolved (>1 pc; Russeil et al. 2016), enabling us to estimate their age, ionizing flux, and density (e.g., Osterbrock & Ferland 2006; Anderson et al. 2014). These regions can be identified in mid-infrared (MIR) observations as bubble- or shell-like structures, which are often asymmetrical in shape (Comeron 1997) and are formed as a result of winds and radiation from the massive central stars. The stellar winds and radiation result in expanding HII regions, which sweep material on their shells and consequently alter the magnetic field morphology of their environment (due to flux freezing) compared to the rest of the parent cloud.

While HII region age estimates are required for studying star formation, their ages can be underestimated if magnetic fields are ignored (Chen et al. 2022). This underestimation of age is due to the fact that strong magnetic fields resist the HII expansion perpendicular to the field direction (which may also result in ovoid-shaped bubbles; Chen et al. 2022). The relative orientation of magnetic field with the expansion of the HII region influences not only the density of the shell but also its fragmentation and core formation (Chen et al. 2022). Some studies have examined the role and significance of magnetic fields in cloud evolution and star formation and have shown that the magnetic fields can be aligned tangential to the shells of evolved HII regions (e.g., Pereyra & Magalhaes 2007; Tang et al. 2009; Chen et al. 2012, 2017; Santos et al. 2014; Fissel et al. 2016; Soam et al. 2017, 2018; Eswaraiah et al. 2017; Pattle et al. 2018; Dewangan et al. 2018; Eswaraiah et al. 2020; Könyves et al. 2021; Devaraj et al. 2021; Fernández-López et al. 2021; Hoang et al. 2022; Chung et al. 2022). This tangential field morphology is also predicted in some theoretical simulations (Krumholz et al. 2007; Henney et al. 2009; Arthur et al. 2011; Ntormousi et al. 2017). However, the complete morphology and role of magnetic fields in relation to HII regions are not yet well understood.

If HII regions orient and order the field lines tangential to them, this will also appear as tangential magnetic fields when projected onto the plane of the sky and will be accompanied by higher polarization fractions. These ordered field lines will experience less deviation from tangential morphology, leading to less depolarization and a higher polarization fraction. To better understand the morphology of magnetic fields associated with HII regions, here we study the magnetic fields in the NGC 6334 molecular cloud and its HII regions. In this study, we investigate the presence or absence of tangential magnetic field morphology in HII regions, as well as whether the presence of such fields is accompanied by an increase in polarization fraction. Determining the presence of this morphology may reveal the significance of HII regions in the evolution of cloud's magnetic fields. Furthermore, by understanding how HII regions may influence the morphology of magnetic fields in their parental cloud, we may also be able to determine the initial magnetic field morphology of the parental cloud prior to its evolution. Knowing this initial magnetic field morphology allows us to compare it to the magnetic field morphology predicted by cloud-formation scenarios.

Numerous HII regions are associated with NGC 6334, which is a massive star-forming molecular cloud, on the inner edge of the Sagittarius-Carina arm (Russeil et al. 2012), with core masses ranging from 200–2000$M_\odot$ (Zernickel et al. 2013) and a total mass of a few $10^5 M_\odot$ (Andre et al. 2016). These HII regions have influenced the gas dynamics in NGC 6334 (Schneider et al. 2020) and some of them are well known and optically observed (e.g., Gum 1955; Persi & Tapia 2008). The presence of numerous HII regions along the filamentary NGC 6334 molecular cloud, which were initially detected by Rodriguez et al. (1982) and have been extensively studied, is not unique to this region and has been similarly observed in other molecular clouds (e.g., NGC 6357; Russeil et al. 2010). Rodriguez et al. (1982) estimated the luminosity of the HII regions within NGC 6334 and identify the zero-age main-sequence (ZAMS) stellar type required to generate the estimated luminosity (see their Table 2). Subsequent studies identify a number (or cluster) of stars that may have contributed to the formation of the NGC 6334 HII regions (e.g., Tapia et al. 1996).

NGC 6334 and its subregions have been observed with various radio, millimeter, and submillimeter facilities, including the Atacama Large Millimeter/submillimeter Array (e.g., Sadaghiani et al. 2020; Cortes et al. 2021), the Very Large Array (VLA; e.g., Rodríguez et al. 2014), and the

Submillimeter Array (e.g., Zhang et al. 2014). NGC 6334 is actively forming stars and includes a ∼10 pc filament (main ridge; Loughran et al. 1986; Russeil et al. 2010; Shimajiri et al. 2019) with an average density significantly higher than most filaments observed in the Gould Belt (Andre et al. 2016). Wu et al. (2014) determined a parallax distance of $1.35^{+0.15}_{-0.13}$ kpc for NGC 6334, ∼20% smaller than its near kinematic distance of 1.7 kpc (Wu et al. 2014) and photometric distance of 1.74 ± 0.31 kpc (Neckel 1978).

To investigate the magnetic field morphology of NGC 6334 and its HII regions, we observe polarized dust emission at 850 μm, using the James Clerk Maxwell Telescope[91] (JCMT) near the summit of Maunakea. Probing the plane-of-sky magnetic field ($B_{\rm POS}$) morphology using polarized dust emission is possible due to the alignment of the short axis of amorphous dust grains (e.g., Draine 2009) with the magnetic field, which has been observed at various wavelengths (e.g., Pattle & Fissel 2019). This alignment is explained through radiative torques (Draine & Weingartner 1997; Lazarian 2007; Lazarian & Hoang 2007; Andersson et al. 2015; Hoang & Lazarian 2016).

Previously, Arzoumanian et al. (2021, hereafter Paper I) studied the magnetic fields within NGC 6334 and the region's filamentary nature. We focus on its HII regions in this study. We discuss our JCMT polarization observations and the previously observed HII regions associated with NGC 6334 in Section 2. In Section 3, we discuss the methodology that we use to characterize the magnetic field morphologies of the HII regions and discuss their impact on the cloud's magnetic field. In Section 4, we compare the magnetic pressure and tension with the gas, radiation, and dynamic pressures in these regions and further explore techniques for identifying these HII regions based on their dust polarization properties. Section 5 summarizes our approach and findings.

2. Observational Data

In this section, we first discuss the JCMT SCUBA-2/POL-2 (Bastien et al. 2011; Holland et al. 2013; Friberg et al. 2016) polarimetric observations of NGC 6334 at 850 μm, taken as part of the *B*-fields In STar-forming Region Observations (BISTRO) survey (Ward-Thompson et al. 2017). We then present the HII regions of NGC 6334 as obtained from a variety of previously published catalogs.

2.1. JCMT BISTRO Observations

The 850 μm dust polarized emission observations were carried out under dry weather conditions with the atmospheric opacity ranging between 0.03 and 0.07 at 225 GHz. The data were reduced using the pol2map[92] reduction code. Observational and data reduction procedures are discussed in detail in Paper I, which also includes these data.

The observations have a spatial resolution of 14″ (half-power beam-width of the JCMT at 850 μm). The maps of Stokes *I* (the total dust thermal continuum emission), Stokes *Q*, and Stokes *U* are re-projected onto Cartesian grids with pixel sizes of 4″. The NGC 6334 molecular cloud is depicted in Figure 1 with pixel size of 4″. The Stokes *I*, *Q*, and *U* maps and their associated uncertainties are discussed in detail in Paper I.

[91] https://www.eaobservatory.org/jcmt/
[92] http://starlink.eao.hawaii.edu/docs/sc22.htx/sc22.html

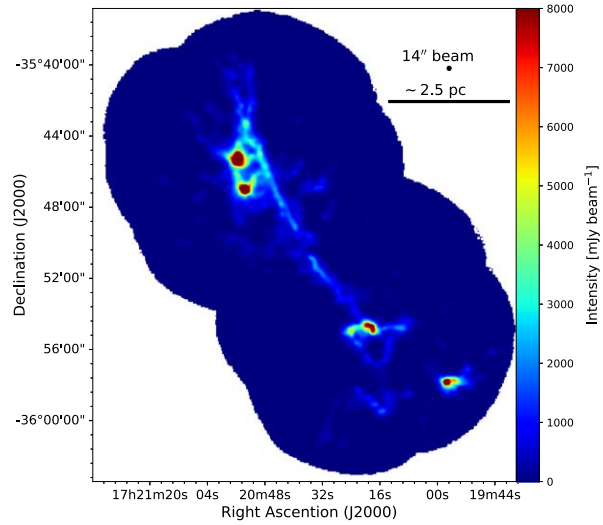

Figure 1. NGC 6334 at 850 μm with a pixel size of 4″. The color image shows Stokes *I* without any selection criteria applied. The cloud is composed of a main ridge (∼10 pc long filament) along with dense clumps and cores. Evidence of HII shells is also visible in the Stokes *I* map.

We obtain the polarization angle (ψ) and the initial polarized intensity ($\rm PI_{INIT}$), using the Stokes parameters in the following equations:

$$\psi = 0.5\ \arctan\left(\frac{U}{Q}\right),$$
$$\times\ \rm PI_{INIT} = \sqrt{Q^2 + U^2}, \quad (1)$$

where the polarization angle is determined according to the IAU convention (from north to east in the equatorial coordinate system). The $B_{\rm POS}$ lines are perpendicular to the polarization lines, and their orientation ($\chi_{B_{\rm POS}}$) is obtained using

$$\chi_{B_{\rm POS}} = \psi + 90^\circ. \quad (2)$$

The parameter $\rm PI_{INIT}$ is positively biased due to the squaring of the uncertainties in Q (denoted by δQ) and U (denoted by δU). We debias $\rm PI_{INIT}$ and obtain the debiased polarization fraction (PF) as follows (e.g., Serkowski 1962; Wardle & Kronberg 1974):

$$\rm PI = \sqrt{Q^2 + U^2 - 0.5(\delta Q^2 + \delta U^2)},$$
$$\rm PF = \frac{PI}{I}. \quad (3)$$

This debiasing approach has been successfully used in previous studies for signal-to-noise ratios (S/Ns) higher than 3 (e.g., Vaillancourt 2006; Plaszczynski et al. 2014; Montier et al. 2015; Hull & Plambeck 2015; Pattle et al. 2019, 2021; Doi et al. 2020). Subsequently, we find the uncertainties of the debiased polarization parameters as follows:

$$\delta\rm PI = \frac{\sqrt{(Q\delta Q)^2 + (U\delta U)^2}}{\rm PI},$$
$$\delta\rm PF = \rm PF\sqrt{\left(\frac{\delta PI}{PI}\right)^2 + \left(\frac{\delta I}{I}\right)^2},$$
$$\delta\psi = 0.5\frac{\sqrt{(U\delta Q)^2 + (Q\delta U)^2}}{PI^2}, \quad (4)$$

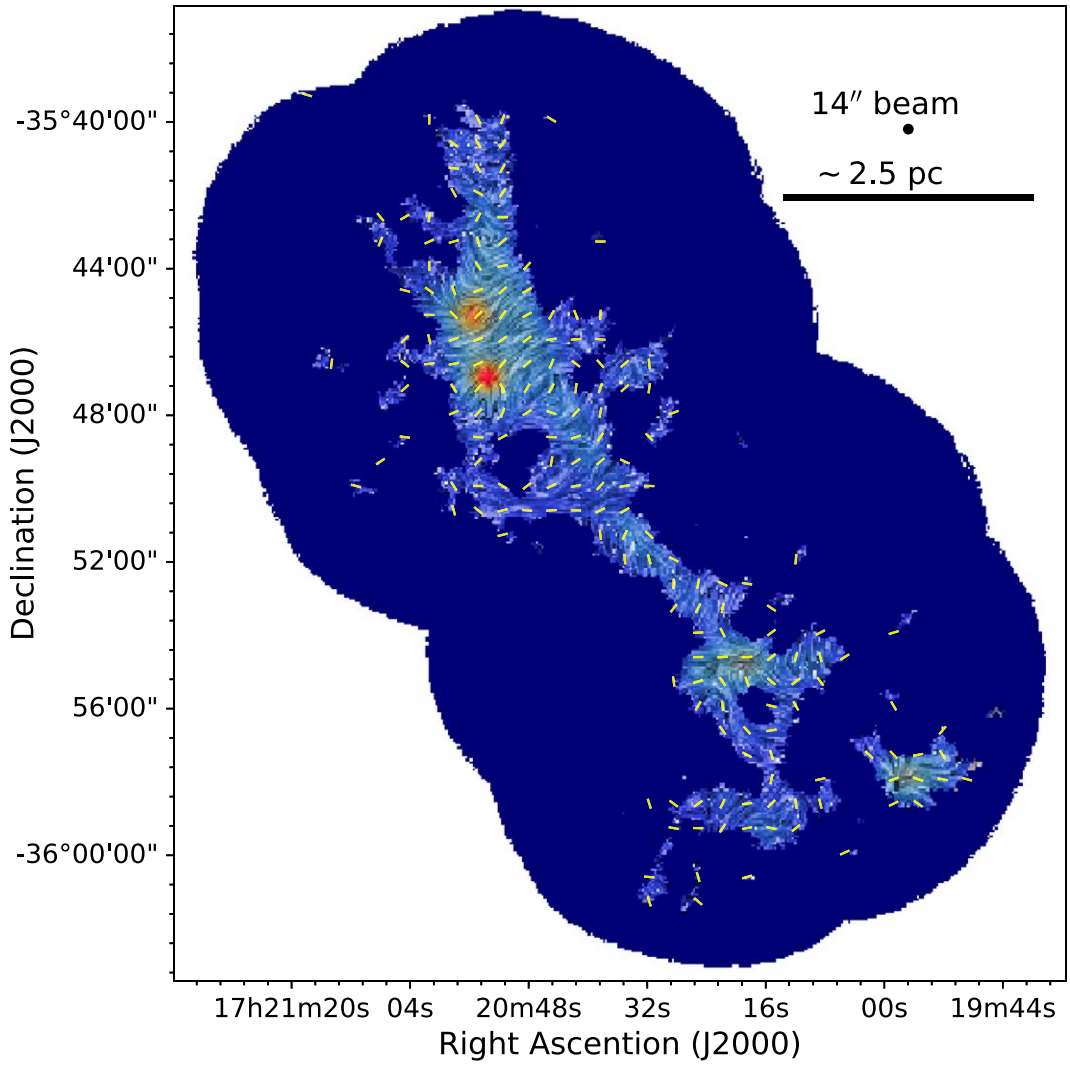

Figure 2. Magnetic field lines associated with NGC 6334 at 850 μm. The background color image illustrates the Stokes I map, and the drapery lines depict the plane-of-sky magnetic field lines in this region as obtained using the line integration convolution technique. The short yellow lines represent the $B_{\rm POS}$ orientations (all of the same length), every 10 pixels.

where the δ shows the uncertainty or the $\sqrt{\text{variance}}$ in each observed parameter. In this study, we use $\mathrm{S/N}(I)=\frac{I}{\delta I} > 10$ and $\mathrm{S/N(PI)}=\frac{\mathrm{PI}}{\delta \mathrm{PI}} > 3$ as data selection criteria, following Paper I. Figure 2 illustrates the overall magnetic field morphology of NGC 6334 using the line integration convolution technique (Cabral et al. 1993). The background color image illustrates the Stokes I map and the drapery lines depict the magnetic field lines. The short yellow lines represent the plane-of-sky magnetic field orientations, every 10 pixels.

2.2. Observed HII Regions

HII regions are best identified and confirmed using radio recombination lines (RRLs) or Hα observations. However, surveys by Bania et al. (2010) and Anderson et al. (2011) demonstrated that MIR observations can be used to identify these regions, which appear as a bubble-like structure in $\sim$22 μm observations surrounded by a shell-like structure at $\sim$12 μm wavelength. Traditionally the HII regions in NGC 6334 were named A to E when observed in radio (Rodriguez et al. 1982), and I to V when observed in far-infrared (FIR; McBreen et al. 1979). For a complete list of all observed HII regions in NGC 6334, we use the Wide-field Infrared Survey Explorer (WISE;[93] Anderson et al. 2014) and Simpson et al. (2012) catalogs (observed in MIR). We refer to the HII regions identified in the WISE and Simpson et al. (2012) catalogs as WISE and Simpson bubbles, respectively.

The WISE catalog compiles more than 8000 confirmed and candidate HII regions in the Galactic disk that were observed by the WISE satellite in the 12 μm and 22 μm bands (Anderson et al. 2014, 2015). The HII bubbles in the WISE catalog are categorized as known (K), groups (G), candidates (C), and radio quiet candidates (Q). Known regions are those that have been observed in either RRL or Hα. When candidate HII regions are spatially associated with known HII regions, they are referred to as groups. A radio quiet candidate is a region that is normally undetectable by radio continuum surveys due to their low sensitivity, but that is detected by WISE (with the 6 mJy sensitivity of WISE at 22 μm). Candidates (C and Q) are typically found to be HII regions 95% of the time (Anderson et al. 2014, 2015, 2018).

[93] http://astro.phys.wvu.edu/wise/

Additionally, we use the HII catalog from Simpson et al. (2012) to further locate regions in NGC 6334. The bubbles identified by Simpson et al. (2012) are part of the citizen science Milky Way Project (MWP)[94] in which online volunteers determined the location of the bubbles using Spitzer observations in the 8 μm and 24 μm bands. The WISE and Simpson catalogs identify HII regions with slightly different centers and radii. This is likely because these bubbles are not perfectly spherical, and the two studies use different methods to determine the radii and shell thickness of HII regions (based on their MIR characteristic morphology). Anderson et al. (2014; WISE survey) used circles to identify the regions, whereas Simpson et al. (2012; Simpson catalog) relied on volunteer assistance to associate elliptical objects with these regions (after which the regions are chosen based on their selection number[95] and an effective radius is determined to describe the radius of each one).

The WISE and Simpson bubbles associated with our observations are illustrated in Figure 3 and listed in Tables 1 and 2. The WISE bubbles are numbered W1 to W8, depicted with red circles in Figure 3. The Simpson bubbles are denoted by the letter S and are numbered similarly to the corresponding WISE bubbles; if a WISE and a Simpson bubble depict a similar bubble in the sky, they are numbered identically (for example, W5 and S5); if a Simpson bubble is nested within a WISE bubble (at a similar location but with a significantly smaller radius), it is numbered identically as the WISE bubble but with the suffix "a" (for example, W7 and S7-a).

Table 1 lists the WISE bubbles along with their equatorial coordinates, radius, distance (parallax measurements by Wu et al. 2014), category, and the local standard of rest velocity (kilometers per second). We note that the mean molecular and ionized gas velocities of NGC 6334 are $-4\,\mathrm{km\,s^{-1}}$ (Russeil et al. 2016) and $-3\,\mathrm{km\,s^{-1}}$ (Caswell & Haynes 1987), respectively. Bubbles W4 to W8 are "known" bubbles, identified by Quireza et al. (2006) using Carbon RRL (CII) at 3.5 cm. The physical scale of Bubble W4 is comparable to that of the NGC 6334 cloud, and it likely contributed to the formation of NGC 6334 (Fukui et al. 2018); consequently, it is not extensively discussed in our analysis of HII regions within the cloud. The Simpson bubbles are listed in Table 2 along with their equatorial, effective radius (R_{eff}), effective thickness (Th_{eff}), inner and outer diameters (along the δ and α axes), eccentricity, and position angle of the ellipsoid bubble. Each of the Flags 1, 2, and 0 denotes a distinct bubble type. Flag 1 denotes bubbles with smaller bubbles on their edges, Flag 2 represents those found within larger bubbles, and Flag 0 indicates neither of these two.

3. HII Magnetic Field Morphologies

HII regions can push away their surrounding interstellar medium (and the frozen-in field lines), resulting in tangential magnetic field (radial polarization[96]) patterns. Moreover, the magnetic field lines surrounding these bubbles are likely to have been compressed (e.g., Eswaraiah et al. 2020) and ordered, potentially resulting in increased polarization fractions. These effects can be seen in our observations. The plane-of-sky magnetic field lines depicted in Figure 3 indicate tangential fields (radial polarization) associated with some of these HII regions. This field morphology is evident in W5 (S5), as illustrated in the inset of Figure 3, representing equally sized magnetic field lines in a zoomed-in view of this bubble. This wrapping of the field lines appears as a periodic polarization angle pattern along the circumference of each bubble, resulting in contiguous areas of below-90° and above-90° magnetic field angles surrounding each bubble. Figure 4 illustrates signatures of this behavior in $\chi_{B_{\mathrm{POS}}}$ (cyclic orientations of B_{POS} lines changing from blue to red to blue to red in the figure), which is characteristic of tangential field morphologies (wrapping of field lines around a bubble). In this figure, blue denotes a magnetic field angle less than 90°, and the red color shows a magnetic field angle greater than 90° (in the IAU convention).

Furthermore, theoretical studies (e.g., Krumholz et al. 2007) demonstrate that HII regions can influence and alter the magnetic field morphology of their parental molecular cloud. Krumholz et al. (2007) simulated the evolution of magnetized HII regions, resulting in tangential magnetic field lines. Figure 5 depicts their resulting field morphology after approximately 0.53 Myr with an initial magnetic field strength of 14.2 μG. We examine the HII magnetic field morphologies and their polarization fractions in this section.

3.1. Identifying Field Morphologies: Methodology

To investigate the polarization patterns associated with the HII bubbles and determine whether they represent a tangential magnetic field pattern, we transform the polarization frame of reference for each bubble individually and define radial Stokes parameters Q_r and U_r. In this reference frame, a polarization line along the radius of the bubble has a zero polarization angle. At each position (α, δ) about the bubble center (α_0, δ_0), we obtain Q_r and U_r using:

$$\begin{aligned} Q_r &= +Q\cos 2\phi + U\sin 2\phi, \\ U_r &= -Q\sin 2\phi + U\cos 2\phi, \end{aligned} \tag{5}$$

where $\phi = \arctan\frac{\alpha-\alpha_0}{\delta-\delta_0}$ is the polar angle of a given position with respect to the center of the bubble in equatorial coordinates. The angle ϕ is zero when pointing toward north and increases toward east. We then determine the average Q_r and U_r at fixed distances from the bubble center (i.e., radial profile of $\langle Q_r\rangle$ and $\langle U_r\rangle$, averaged within thin, 2 pixel-wide annuli around the bubble). A positive $\langle Q_r\rangle$ value indicates that a shell demonstrates a radial polarization pattern on average, whereas a negative value hints to a tangential polarization pattern. U_r represents polarization at a ±45° angle to the radial direction. Therefore, $\langle U_r\rangle = 0$ indicates radial or tangential polarization at that radius.

This formalism enables us to more easily identify radial polarization (tangential magnetic field patterns) associated with individual bubbles. Schmid et al. (2006) previously employed this technique to study the radial polarization associated with Uranus and Neptune. They found that the technique was particularly effective in reducing uncertainties caused by systematic errors in the data reduction process. Additionally, Canovas et al. (2015) used the technique to investigate the polarization of protoplanetary disks.

[94] http://www.milkywayproject.org
[95] Hit rate.
[96] We use the terms "radial polarization" and "tangential magnetic field" interchangeably in this study, as the field lines are perpendicular to the polarization lines.

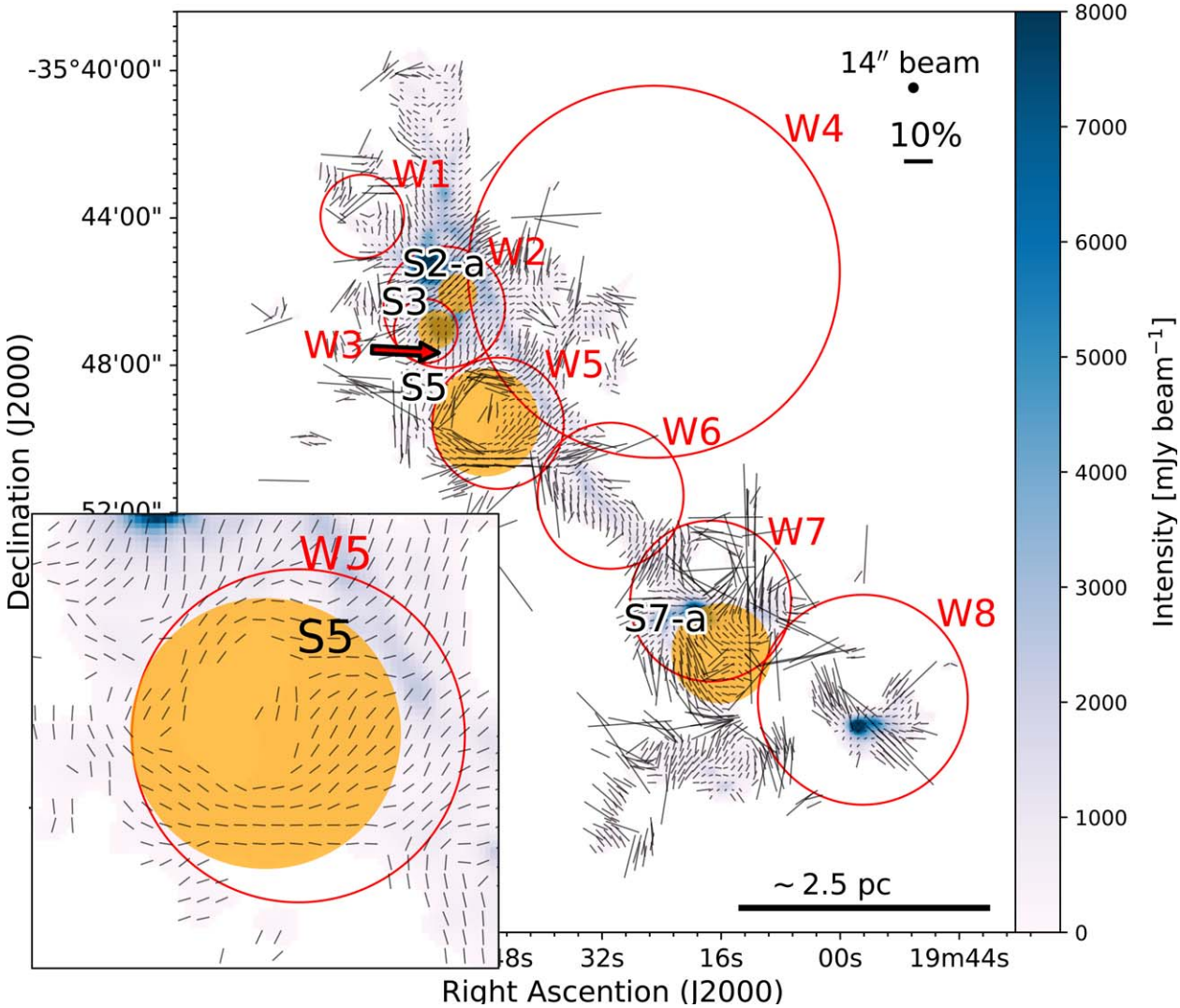

Figure 3. HII regions associated with NGC 6334. The background color image shows the Stokes I map. The black lines represent the plane-of-sky magnetic field orientation for a 12″ pixel-sized map (in order to make it appear less crowded visually). The length of each field line is proportional to the polarization fraction. The red circles depict the WISE bubbles, which are numbered with a red font on their top-right side. The orange disks represent the Simpson bubbles, which are labeled in black font in their upper-left corner. The inset shows a zoomed-in view of W5 (and S5), which clearly exhibits tangential field (radial polarization) lines as equal-length segments relative to the bubble.

To study $\langle Q_r \rangle$ and $\langle U_r \rangle$ more efficiently and to determine the radial polarization patterns, we define θ_r as follows:

$$\theta_r = 0.5 \times \arctan\left(\frac{\langle U_r \rangle}{\langle Q_r \rangle}\right). \quad (6)$$

If a shell exhibits radial polarization on average (with positive $\langle Q_r \rangle$ and near zero $\langle U_r \rangle$ values), then $\cos(\theta_r)$ should be close to 1. We look for radii with $\cos(\theta_r) > 0.95$ (allowing for 5% total variation or uncertainty) including the error bars, to identify shells with radial polarization patterns. Appendix A contains a discussion of the method used to calculate the error bars.

3.2. Polarization Pattern of HII Regions in NGC 6334: Results

Figures 6, 7, and 8 illustrate the radial profile of both $\cos(\theta_r)$ and the mean polarization fraction for each bubble (averaged in each annulus with a thickness of 8″, or two pixels). In these figures, the left panel illustrates $\cos(\theta_r)$ and the mean polarization fraction with blue and red marks, respectively. The right panel shows a zoomed-in view of the magnetic field lines of each bubble overlaid on Stokes I. The dashed vertical and horizontal lines indicate the radius of each bubble (the Radius and $R_{\rm eff}$ columns in Tables 1 and 2, respectively) and $\cos(\theta_r) = 0.95$, respectively. The blue markers indicate the total number of pixels (that satisfy the selection criteria of S/N (I)>10 and S/N(PI)>3) in each annulus. Some bubbles have boundaries outside of the NGC 6334 cloud in regions with the lowest density and fewest pixels.

We find that radial polarization in bubbles is accompanied by a higher polarization fraction, implying that HII regions have ordered and compressed the magnetic field lines. A statistical study involving a large number of bubble polarization observations is necessary to determine if the amount of increase in polarization fraction can quantitatively reveal information about the physical properties of the bubbles (e.g., ratio of regular to random field or compression factor).

To facilitate discussion of these findings, we divide this section into two subsections: bubbles that exhibit radial polarization at one or more radial distances, and bubbles that

Table 1
Bubbles Found in the WISE Catalog Associated with NGC 6334

Number	Name	α (° J2000)	δ (° J2000)	Radius (″)	Dist (kpc)	Category	V_{LSR} (km s^{-1})
W1	G351.479 + 0.643	260.268	−35.734	68.0	⋯	Q	⋯
W2	G351.424 + 0.65	260.223	−35.775	99.0	⋯	G	⋯
W3	G351.42 + 0.637	260.233	−35.786	52.0	⋯	Q	⋯
W4	G351.383 + 0.737	260.106	−35.759	303.0	1.3	K	−3.4
W5	G351.367 + 0.64	260.193	−35.828	107.0	1.3	K	−3.4
W6	G351.311 + 0.663	260.13	−35.86	119.0	1.3	K	−3.4
W7	G351.246 + 0.673	260.074	−35.908	131.0	1.3	K	0.6
W8	G351.17 + 0.704	259.989	−35.953	171.0	⋯	K	0.5

Note. The name, R.A. (α), and decl. (δ) for the center of each bubble are indicated. The velocities (V_{LSR}) are obtained from Quireza et al. (2006) and distances (dist) from Wu et al. (2014) using parallax measurements. The bubble categories are known (K), radio quiet (Q), and group (G), as identified in the WISE catalog.

do not. Figures 6 and 7 illustrate bubbles with radial polarization at one or more radial distances. When a bubble is associated with a Simpson bubble, a middle panel is added to display the results for the Simpson bubble (Figure 7). Figure 8 illustrates bubbles with no radial polarization patterns at any radial distance.

3.2.1. Bubbles with Radial Polarization Signatures

Radial polarization at one or more radial distances can be seen in bubbles W1 and W5 to W8, with W5 and W7 having corresponding Simpson bubbles (S5 and S7-2). W1, W6, and W8 (with no corresponding Simpson bubbles) are illustrated in Figure 6, while W5 and W7 are depicted in Figure 7.

Bubble W1 is classified as a radio quiet HII region in the WISE catalog, with an unidentified distance by the WISE catalog or Wu et al. (2014). However, its dust morphology indicates that W1 is associated with NGC 6334. When the location of W1 is compared with the morphology of submillimeter dust observations shown in Figure 3, it appears as though the center of this bubble, as identified in the WISE catalog, is slightly shifted relative to the center location where the effects of bubble expansion on dust can be observed. At 45″ radial distance, the polarization exhibits a radial pattern, with a peak in polarization fraction (around 7%), as illustrated in the upper-left panel of Figure 6. Following that at greater distances, polarization lines diverge from radial angle and the polarization fraction decreases.

Bubble W6 is categorized as a known bubble, and it is approximately the same distance away from us as NGC 6334. When projected onto the plane of the sky, W6 appears to contain a ∼1 pc-long filament. The middle-left panel of Figure 6 indicates tangential polarization near the center of the bubble (along the filament) and radial polarization between radii of ∼60″ and 110″. This radial polarization range also exhibits higher polarization fractions (6%–7%). As depicted in Figure 3, W6 appears in contact with W5 to the northwest and W7 to the southeast (when projected onto the plane of the sky). Therefore, at greater distances beyond the radius of W6, the effects of radial polarization associated with W5 and W7 (higher polarization fractions) can be seen.

Although Bubble W8 is classified as a known bubble, neither the WISE catalog nor the study by Wu et al. (2014) indicate its distance. However, the dust morphology suggests that W8 should be directly associated with NGC 6334. The lower-left panel of Figure 6 indicates radial polarization in the radius range of 160″–180″, along with locally maximal polarization fraction (∼9%).

Bubble W5, a known bubble, has the same distance from us as NGC 6334. The magnetic field lines associated with this bubble clearly demonstrate the impact of the HII region, as illustrated in the inset of Figure 3. The upper-left panel of Figure 7 shows radial polarization in the radius range of ∼60″–90″ with on-average higher polarization fraction (∼6%–8%). This is similar to the values in the upper-middle panel of Figure 7 for S5 (radii of ∼50″–85″ and PF of ∼6%–10%), where the small difference is due to the slight difference in radius and center for W5 and S5. The observed field lines appear to be more consistent with S5 than W5. At radial distances greater than the radius of the bubble, the polarization pattern becomes nonradial, and the polarization fraction decreases by a factor of ∼2, indicating that the field lines are less ordered.

Bubble W7 is at the same distance as NGC 6334 and in the known category. The presence of radial polarization and an increase in the polarization fraction can be seen in this bubble at $r \simeq 90''$–$100''$. Additionally, at distances greater than the radius of W7, the polarization lines exhibit a higher polarization fraction or radial polarization due to the influences of W6 and W8.

W7 has a bipolar morphology (suggested by Harvey & Gatley 1983, based on the dust temperature studies of the two lobes) and on its south side is associated with S7-a, which is part of a Herbig–Haro object (southern lobe; Bohigas 1992). This bipolar morphology is likely caused by the confinement of an HII region within a flattened-like (or torus-like) molecular gas structure (Kraemer & Jackson 1999), which allows the ionized gas to escape only in the north and south directions (extending 2′; Rodriguez et al. 1988). This bipolar structure is also visible in our observations; the magnetic field morphology of W7 resembles a radial polarization pattern for two lobes (to the north and south of its center), with their radial polarization features coinciding near the center of W7, as illustrated in the lower-right panel of Figure 7.

The southern lobe of W7 can be studied using the S7-a bubble. S7-a exhibits a radial polarization pattern at $r \simeq 80''$, as illustrated in the lower-middle panel of Figure 7. However, the polarization fraction increases at radii greater than this value, as the polarization fraction is also influenced by W8 at these radii.

No distinct HII region has been identified in the WISE or Simpson catalogs as being directly associated with the northern lobe of W7. We approximate the bipolar structure (shown with black circles in Figure 9) based on the 6 cm observations of Rodriguez et al. (1988), in which the northern lobe appears slightly shifted to the south in comparison to the tangential field lines (radial polarization) visible in our data. As a result, we

Table 2
Bubbles Identified by Simpson et al. (2012) Associated with NGC 6334

Number	α(° J2000)	δ(° J2000)	$R_{\rm eff}$ (′)	$\rm Th_{eff}$ (′)	InnXDia (′)	InnYDia (′)	OutXDia (′)	ϵ	PA(°)	Hit	Flag
S2-a	260.214	−35.768	0.50	0.61	0.630	0.871	1.240	0.691	97	0.16	0
S3	260.225	−35.784	0.49	0.61	0.728	0.730	1.335	0.068	10	0.22	0
S5	260.199	−35.826	1.44	1.46	2.212	2.262	3.676	0.208	33	0.16	1
S7-a	260.067	−35.931	1.33	1.64	1.936	1.986	3.574	0.222	37	0.11	0

Note. The center of each bubble is shown in equatorial coordinates with α and δ. $R_{\rm eff}$ and $\rm Th_{eff}$ represent the effective radius and thickness associated with each bubble. The bubbles are first identified as elliptical shapes (before determination of $R_{\rm eff}$ and $\rm Th_{eff}$) with inner diameters of InnXDia and InnYDia (along the δ and α axes), outer diameter of OutXDia (along the δ axis), eccentricity of ϵ, and ellipse position angle (PA). The "hit rate" of a bubble represents the level of agreement among the MWP users regarding bubble detection and is the ratio of the number of bubbles drawn that qualify as an HII region to the number of times the bubble was detected by the users. The final catalog includes only bubbles with a hit rate of 0.1 or greater. Flags 1, 2, and 0 indicate bubbles with smaller bubbles on their edge, positionally located within a larger bubble, and neither of the two, respectively.

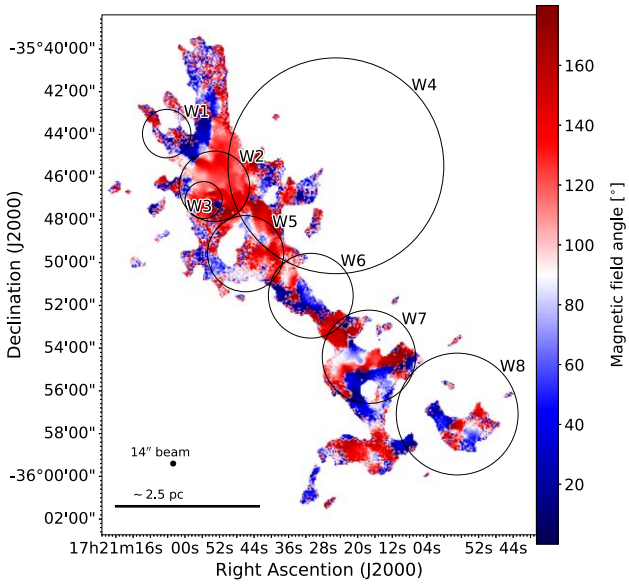

Figure 4. Plane-of-sky magnetic field angles ($\chi_{B\rm POS}$) in NGC 6334. The background color image shows the magnetic field angles in degrees. The angles are in the IAU convention system. The magnetic field angles surrounding some of the bubbles (particularly W5) indicate wrapping of the field lines (changing from blue to red to blue). WISE bubbles are shown with black circles.

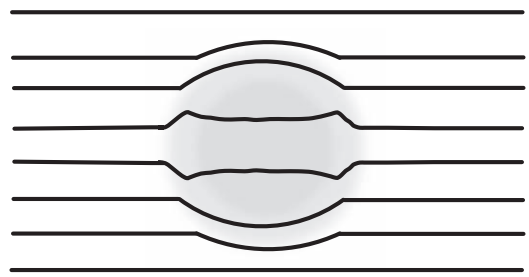

Figure 5. Coevolution of magnetic field lines and HII regions as studied by Krumholz et al. (2007). The black lines and the gray circle show the magnetic field lines and the HII region, respectively. The field lines are pushed by the HII region, resulting in tangential field patterns.

perform our radial polarization analysis on a bubble with a central location of $(\alpha, \delta) = (260\overset{\circ}{.}07, -35\overset{\circ}{.}89)$ and a radius of $\sim 40''$, as estimated by the location of our observed polarization lines. The absence of a distinct HII region for the northern lobe in the catalogs emphasizes the importance of polarization studies in identifying and examining molecular cloud substructures. We discuss this in more detail in Section 4.2, where we investigate the possibility of using polarization properties to identify bubbles that have impacted the field lines.

3.2.2. Bubbles without Radial Polarization

Bubble W2 is classified as "group" in the WISE catalog, with an undetermined distance (to our knowledge). As illustrated in the upper-left panel of Figure 8, the bubble has polarization angles of $\sim 55°(\cos\theta_r \simeq 0.6)$ relative to radial direction and is therefore closer to tangential than to radial lines. These fields are oriented in a single direction (perpendicular to the main ridge) and are likely dominated by the region's high-density cores and/or clumps. This bubble demonstrates a nearly constant polarization fraction of $\sim 2.5\%$. Similarly, compared to other bubbles, the averaged polarization fraction is lower in S2-a (maximum 4% as illustrated in the upper-middle panel of Figure 8), which is nested within W2. We note a small increase in polarization fraction just behind the radius of S2-a, followed by a slight decrease beyond the radius. While the polarization lines appear to have an average $\cos\theta_r \simeq 0.95$ at $20''$ and $30''$, their large error bars indicate a nonradial polarization pattern. The large error bars for $\cos\theta_r$ are due to the fact that the field lines are mostly in one orientation, and thus have different radial angles (relative to radial direction) at various points on the circle.

Bubble W3 is classified as a radio quiet bubble and appears within W2, with an undetermined distance in the WISE catalog. W3 and its corresponding Simpson bubble, S3, do not indicate radial polarization, as illustrated in the lower-left and lower-middle panels of Figure 8. At $r \simeq 35''$, it appears as though the polarization in W3 is approaching radial. However, because the error bars fall below $\cos(\theta_r) = 0.95$, this bubble *does not* pass our criteria for radial polarization, and further analysis is required. As with W2, the polarization lines in W3 appear to be unaffected by the HII region, with a nearly constant polarization fraction ($\sim 2\%$) inside the bubble and a slight increase near the radius of the bubble (up to $\sim 3\%$). W3 (and S3) belong to a dense region of NGC 6334 with active star formation.

While W2 and W3 have unidentified distances in the WISE catalog and do not exhibit radial polarization, observations indicate that they (or their corresponding Simpson bubbles) are associated with NGC 6334. S3 and S2-a are both compact HII regions in the dense part of NGC 6334. A cluster of B0-B0.5 ZAMS stars likely ionize the S2 region (Tapia et al. 1996). S3 is associated with the strongest maser in NGC 6334, H_2O, OH,

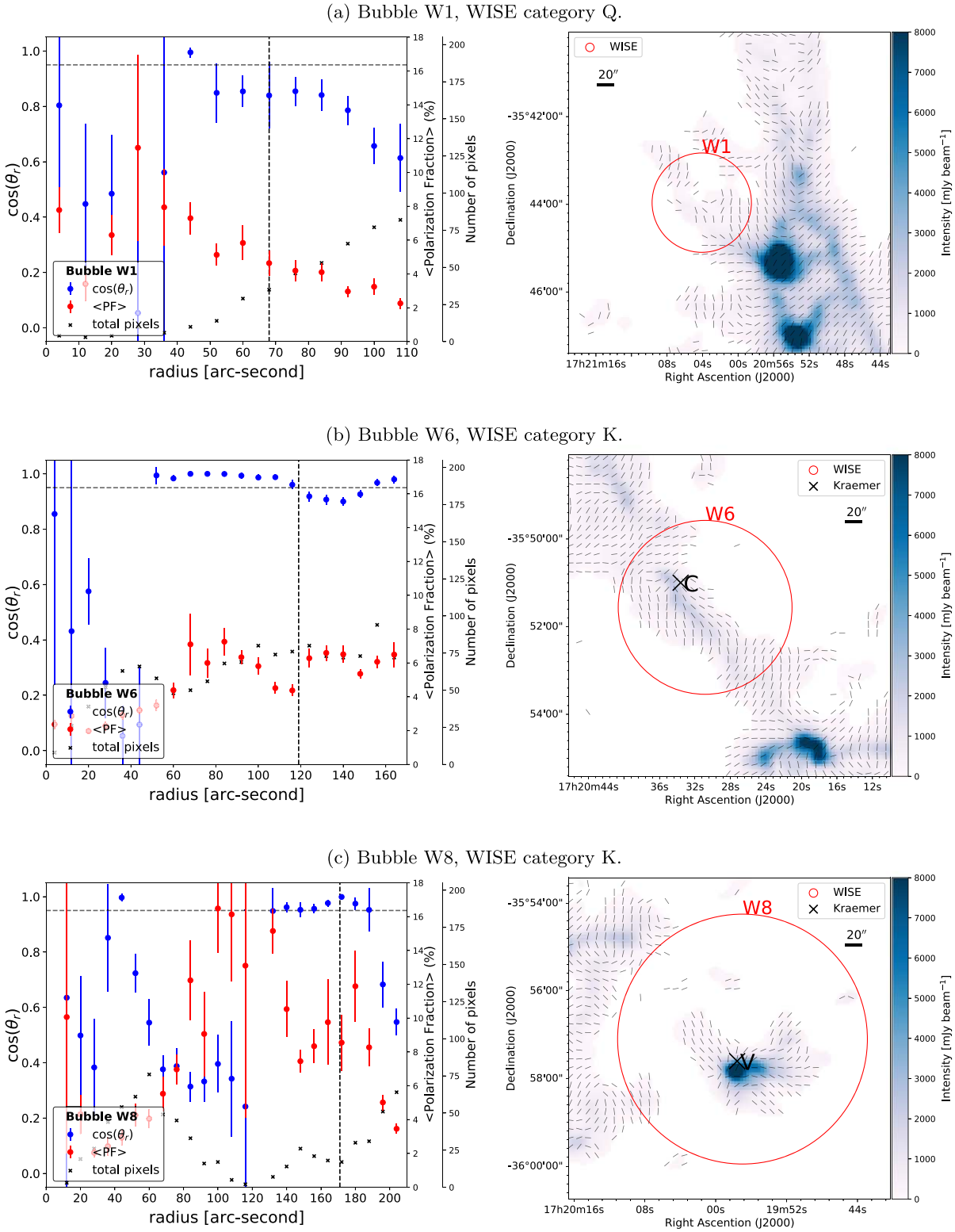

Figure 6. Radial polarization analysis of W1, W6, and W8. Left column: radial profile of $\cos(\theta_r)$ and the mean polarization fraction in each bubble. The dashed vertical and horizontal lines indicate the radius of each bubble and $\cos(\theta_r) = 0.95$, respectively. The blue, red, and black markers indicate $\cos(\theta_r)$, the mean polarization fraction, and the total number of pixels (which satisfy the selection criteria of S/N(I)>10 and S/N(PI)>3) in each shell, respectively. The error bars in polarization fraction represent the standard deviation of the mean. The error bars for the blue markers are discussed in Appendix A. Right column: zoomed-in view of each bubble. The black lines and the background color image represent equally sized magnetic field lines and Stokes I, respectively.

and CH_3OH masers (Moran & Rodriguez 1980; Batrla et al. 1987; Forster & Caswell 1989; Menten & Batrla 1989; Kraemer & Jackson 1999), and a young molecular outflow (Bachiller & Cernicharo 1990).

Finally, we note that as illustrated in Figure 8, bubbles with no evidence of radial polarization have larger error bars (indicating a greater dispersion of Q_r and U_r values within each annulus). As the angle changes with respect to the radius of the

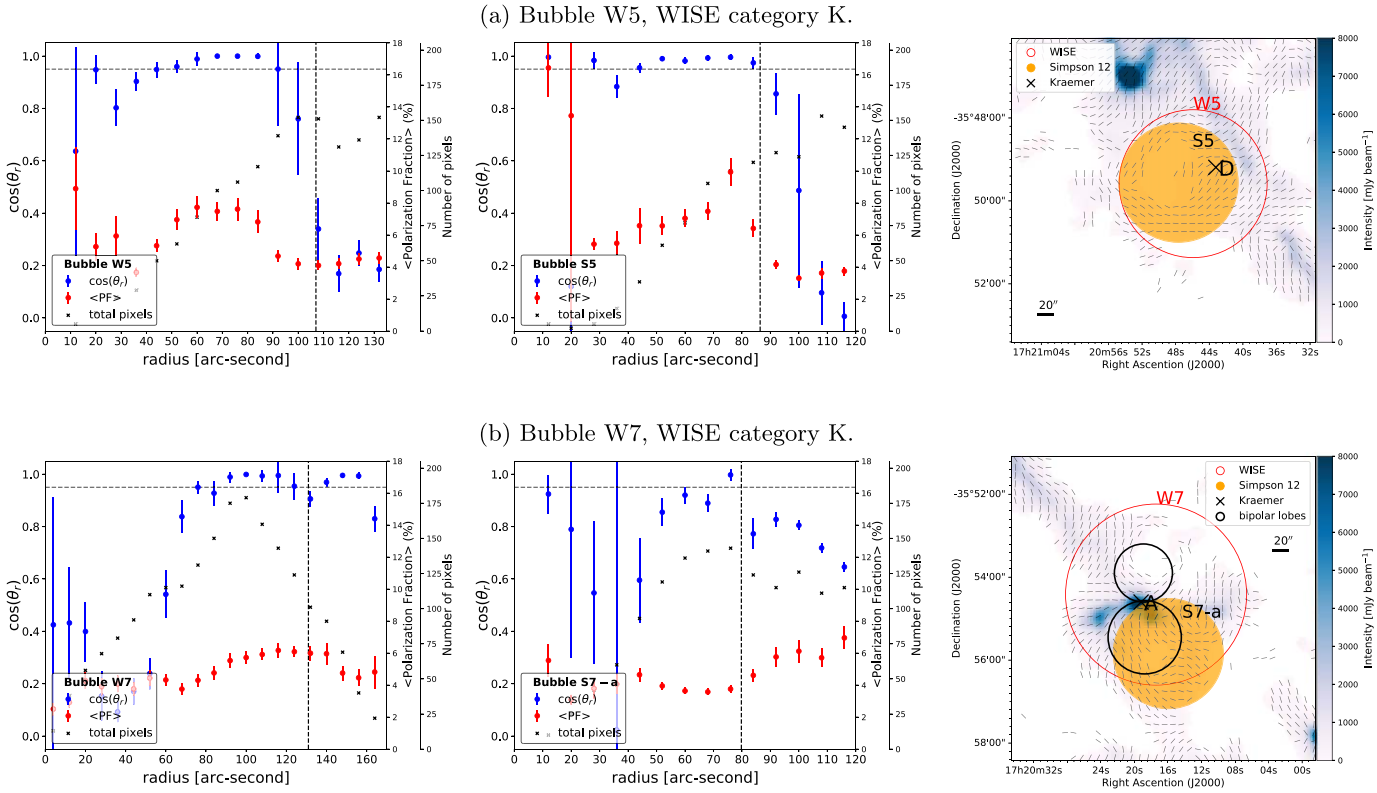

Figure 7. Radial polarization analysis of W5 and W7. Left column: the radial profile of $\cos(\theta_r)$ and the mean polarization fraction in each bubble are shown. The vertical and horizontal dashed lines represent the radius of each bubble and $\cos(\theta_r) = 0.95$, respectively. The $\cos(\theta_r)$ values, the mean polarization fraction, and the total number of pixels (which satisfy the selection criteria of S/N(I)>10 and S/N(PI)>3) in each shell are indicated by the blue, red, and black markers, respectively. The polarization fraction error bars represent the standard deviation of the mean (see Appendix A for $\cos(\theta_r)$ error bars). Middle column: radial polarization analysis of S5 and S7-a, with the same description as the left column. Right column: zoomed-in view of each bubble is shown where the magnetic field lines (of identical size) are overlaid on the Stokes I map. The bipolar nature of W7 is illustrated by the two black circles (see text for details).

bubble, a uniform magnetic field morphology results in greater dispersion, whereas tangential field lines result in small dispersion and error bars.

4. Discussion

All bubbles, except for W2 (and S2-a) and W3 (and S3), exhibit some degree of radial polarization. Table 3 summarizes our findings regarding the magnetic field morphology of HII regions within NGC 6334 as discussed in Section 3. Examining the energy balance associated with these regions is required to better understand magnetic field geometries. Additionally, the polarization patterns of the cloud from small to large scales can reveal important information about substructures within the cloud and the cloud's evolution and/or formation. We discuss these in the following subsections.

4.1. Field Strengths and Energy Comparisons

We employ established equations and observations from the literature to determine the energetic significance of the HII regions in comparison to magnetic fields. These are discussed in greater detail in the following two subsections.

4.1.1. Energy Balance Relations

To estimate the gas thermal pressure ($P_{\rm gas}$), radiation pressure ($P_{\rm rad}$), dynamic pressure ($P_{\rm dyn}$; e.g., Pavel & Clemens 2012; due to bubble expansion), magnetic pressure (P_B; e.g., Pattle et al. 2022), and magnetic tension (T_B; e.g., Boulares & Cox 1990) per unit area (due to curved field lines) of bubbles, we use the following equations (for tangential field lines):

$$P_{\rm gas} = nk_BT,$$
$$P_{\rm rad} = \frac{L}{4\pi r^2 c},$$
$$P_{\rm dyn} = 0.5\rho v_{ex}^2,$$
$$P_B = \frac{B^2}{8\pi},$$
$$T_B = \frac{B^2}{4\pi}, \quad (7)$$

where $n = n_e$, k_B, T, c, r, L, ρ, $v_{\rm ex}$, and B are the electron volume density, Boltzmann constant, gas temperature, speed of light, distance to the center of the bubble, luminosity, mass density, expansion velocity, and magnetic field strength (perpendicular to gas motion), respectively.

While the above-mentioned $P_{\rm rad}$ is used for optically thick regions, studies (Reissl et al. 2018) show that radiation pressure is generally small (or negligible) compared to gravity or gas pressure. We can estimate the magnetic field strength ($B_{\rm resist}$) required to resist the combined effects of gas, radiation, and dynamic pressures, using:

$$P_{\rm B,resist} + T_{\rm B,\ resist} = \frac{3B_{\rm resist}^2}{8\pi} = P_{\rm gas} + P_{\rm rad} + P_{\rm dyn}. \quad (8)$$

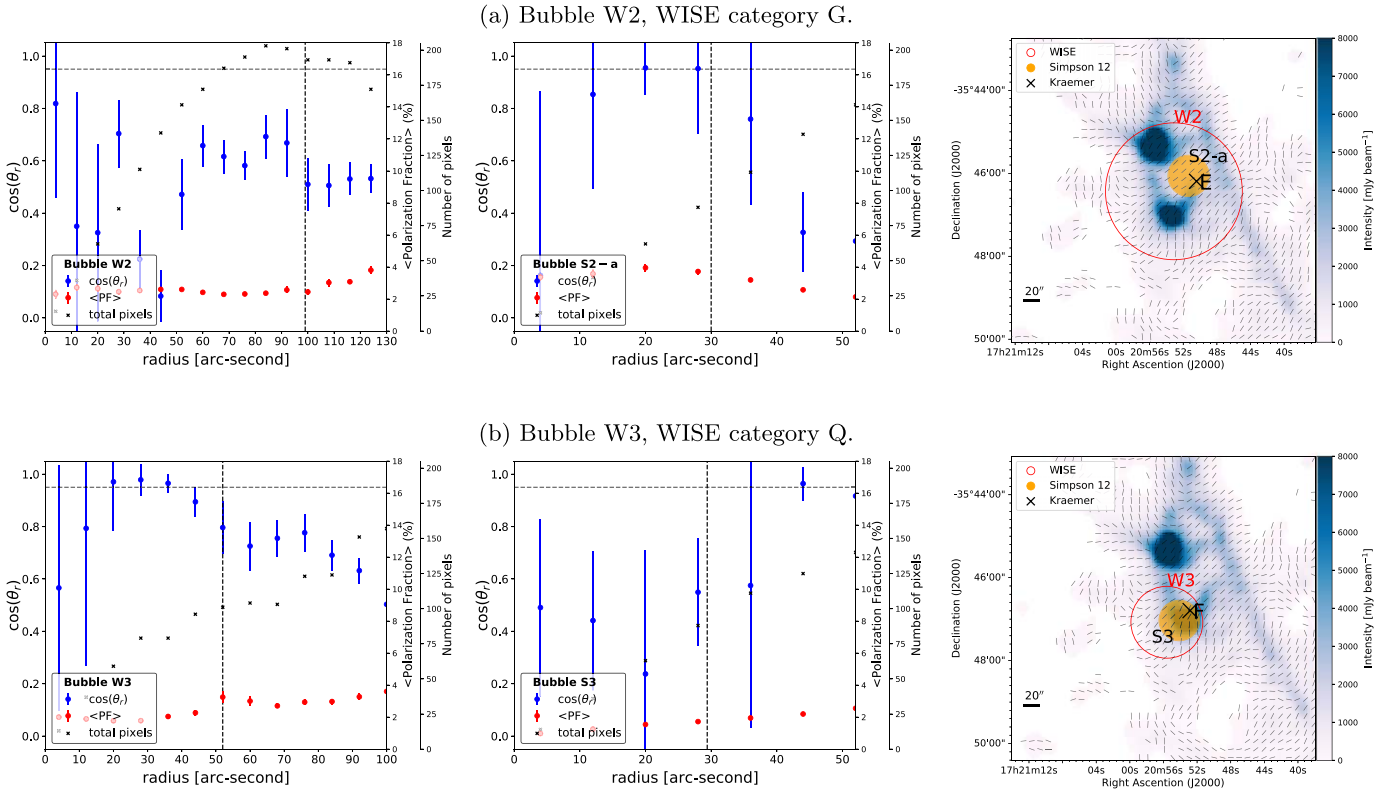

Figure 8. Absence of radial polarization in W2 and W3. Left column: radial profile of $\cos(\theta_r)$ (blue marker) and the mean polarization fraction (red marker) in each bubble are shown. The radius of each bubble and $\cos(\theta_r) = 0.95$ are represented by the vertical and horizontal dashed lines, respectively. In polarization fraction, the error bars represent the standard deviation of the mean. Appendix A discusses the error bars for the blue markers. Middle column: radial polarization analysis of S2-a and S3, with the same description as the left column. Right column: zoomed-in view of each bubble, representing the observed magnetic field lines (of same size).

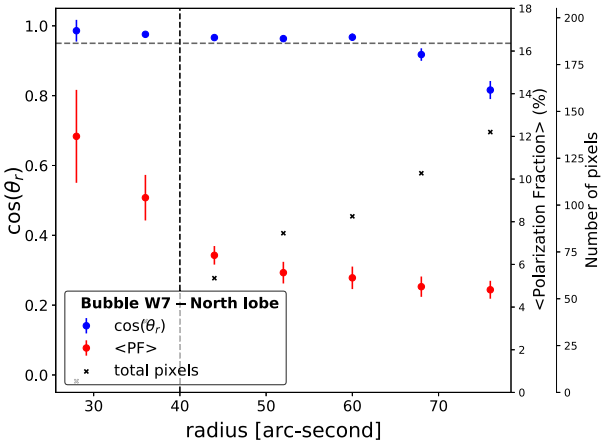

Figure 9. Radial polarization study of W7. The mean polarization fraction, the total number of pixels in each annulus, and $\cos(\theta_r)$ are all shown by the red, black, and blue markers.

Magnetic fields significantly less than this $B_{\rm resist}$ value indicate that the field lines are altered by the HII regions.

4.1.2. Parameter Estimates

Except for W1, all of these bubbles have been previously identified in various observations (e.g., Rodriguez et al. 1982; sources denoted as A to E and source V shown in Figure 10), and their magnetic fields were studied using Zeeman measurements (Sarma et al. 2000; Balser et al. 2016, see Table 3). We note that Kraemer & Jackson (1999) found an anticorrelation between the presence of dense gas and the 6 cm radio flux, which they attribute to gas dispersion by the feedback from the hottest stars. This gas and dust dispersion is also visible in our 850 μm dust observations.

We also employ the parameters listed in Table 4 obtained from Rodriguez et al. (1982) and Russeil et al. (2016). Rodriguez et al. (1982) assumed a temperature of 10^4 K and found the electron volume densities and the HII masses of these sources. Russeil et al. (2016) provided the expansion velocities ($v_{\rm ex}$; see their Table 1). Using the L and n_e values from Rodriguez et al. (1982), a temperature of 10^4 K, and the $v_{\rm ex}$ values, we determine the $B_{\rm resist}$ magnetic field strengths as listed in Table 4 for sources A, C, D, E, and F. These values (except for sources F and E) exceed the observed magnetic field strengths (see Table 3) determined using Zeeman observations (Sarma et al. 2000; Balser et al. 2016) and the Davis-Chandrasekhar-Fermi technique (DCF; Davis & Greenstein 1951; Chandrasekhar & Fermi 1953; associated with substructures on the shells) described in Paper I.

4.1.3. Energy Balance of Individual Bubbles: Bubbles with Radial Polarization Signatures

W1, W5 (and S5), W6, W7 (and S7-a), and W8 all exhibit radial polarization. Among these, W5 (and S5) and W7 (and S7-a) have Zeeman observations associated with them. W5 and S5 correspond to source D, which is identified as an extended, amorphous, and roughly spherical region. Source D contains H_2O maser observations (Moran & Rodriguez 1980) and has a lower molecular hydrogen density than any other source in NGC 6334 (Kraemer & Jackson 1999). We found that a magnetic field strength of 308 μG is required to resist the

Table 3
Summary of Radial Polarization Detection in Bubbles

Bubble	Radius (″)	Source$^{\gamma}$	$B_{\rm LOS}^{\dagger}$ (μG)	$\langle B_{\rm POS}\rangle^{\star}$ (μG)	RP Evidence
W1	68.0			42	at 45″
W2	99.0	E		360	…
S2-a	30	E	−263 ± 78 at 1665 MHz(OH)	…	…
			−340 ± 78 at 1667 MHz(OH)		
			−169 ± 33 at 1420 MHz(Hi)		
W3	52.0	F		415	…
S3	29.4	F		351	…
W5	107.0	D	−60 ± 46 at 1665 MHz(OH)	99	60″ to 90″
			−69 ± 58 at 1667 MHz(OH)		
			−93 ± 13 at 1420 MHz(Hi)		
S5	86.4	D		92	50″ to 85″
W6	119.0	C		144	60″ up to 110″
W7	131.0	A	+148 ± 20 at 1665 MHz(OH)	132	85″ to 110″
			+162 ± 33 at 1667 MHz(OH)		
			+47 ± 15 at 1420 MHz(Hi)		
S7-a	79.8	A		114	at 75″
W8	171.0	V		…	at 160″ and 160″ to 180″

Note. The first, second, and fourth columns show bubble numbers, bubble radius, and magnetic field strength obtained from literature, respectively. The γ represents sources identified by Rodriguez et al. (1982) that were used by Sarma et al. (2000) and Balser et al. (2016) for Zeeman measurements. The †denotes VLA Zeeman measurements by Sarma et al. (2000), with the negative and positive signs indicating directions toward and away from us, respectively. We note that the opposite sign convention of Zeeman measurements is used in Faraday measurements. The fifth column denoted by the $\star$ symbol indicates the approximate plane-of-sky magnetic field strength in the molecular gas surrounding the bubble, using strengths obtained in Paper I. The values listed are the weighted means of the magnetic field strengths estimated by Paper I in filaments overlapping with the bubbles. The final column displays the regions within each bubble that exhibit radial polarization. Balser et al. (2016) determined the magnetic strength of source A to be 190 ± 96 μG and the strength of source D to be approximately 180 to 1200 μG for Source D.

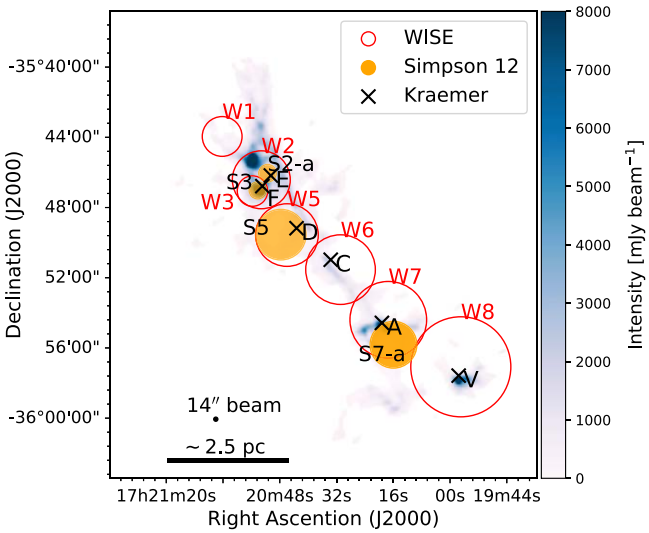

Figure 10. Sources identified by Kraemer & Jackson (1999). The background color image shows the Stokes I map. The orange and red circles show the HII regions identified in the WISE and Simpson et al. (2012) catalogs, respectively. The "x" marks show the sources in Kraemer & Jackson (1999) and used in Sarma et al. (2000) to perform Zeeman measurements.

bubble, which is approximately a factor of 3 greater than the magnetic fields observed with Zeeman or DCF in the vicinity of this region. Therefore, we suggest that the field lines in this region are pushed and influenced by the gas pressure as is evident by the radial polarization (tangential magnetic field) morphology.

The center of W6 coincides with source C. Sarma et al. (2000) found no OH absorption toward the continuum peak of this source to detect Zeeman splitting. This source is nonspherical and likely contains an O7 star (Straw et al. 1989; Kraemer & Jackson 1999). When projected onto the plane of the sky, W6 appears to contain a dense filament, as illustrated in the middle-right panel of Figure 6. This filament can be located inside, at the front, or at the back of the bubble in three dimensions. Magnetic fields run parallel to this filament on the plane of the sky, while the edges of the bubble exhibit radial polarization behavior.

Three explanations can be made for the magnetic morphology of the filament associated with W6: (1) The dense filament may be located on the shell (in 3D; the foreground or background of the bubble) and thus the field lines may appear running parallel to the filament due to their tangential morphology to the shell. (2) The filament may be located within the bubble, showing the general field morphology inside the HII region. (3) The filament may be located inside or on the bubble, with parallel field lines formed by the filament's gas inflow (instead of by the HII region). In this case, the field lines may have transitioned from perpendicular to parallel (with respect to the filament) after gravity took over and material flowed along the filament (e.g., Liu et al. 2018; Busquet 2020; Pillai et al. 2020). Given that the overall magnetic field morphology of NGC 6334 appears to be perpendicular to the larger cloud, we suggest that the third scenario is most likely.

Additionally, given the presence of two dense regions (each containing numerous cores) to the north and south of this bubble (see Figure 11), one could argue that the observed radial polarization pattern (tangential magnetic fields; see Figure 6) at the edge of this bubble is the result of material inflow to these two systems. We refer to these two regions as core-hub systems (see Figure 11), and suggest that these tangential fields are caused by the interaction of the field lines with W6, not by the gravitational pull exerted by the two core-hub systems. This suggestion is backed up by the following arguments: first, we note that a magnetic field strength of 267 μG is required to

Table 4
Sources Studied in Kraemer & Jackson (1999), Rodriguez et al. (1982), and Balser et al. (2016) as Shown in Figure 10

Src	α (°J2000)	δ(°J2000)	Radius (″)	T_k(K)	$n_e(\times 10^3$ cm$^{-3})$	$M_{\rm H\,II}$ ($M_\odot$)	L ($L_\odot$)	$v_{\rm ex}$ (km s^{-1})	$B_{\rm resist}$ μG
A	260.08	−35.91	100	60	20	0.4	8×10^4	15.7	534
C	260.14	−35.85	40	70–80	2	3	7×10^4	14	267
D	260.18	−35.82	40	40–50	3	5	2×10^5	14	308
E	260.21	−35.77	20	50–60	7	1	8×10^4	15•	397
F	260.22	−35.78	10	60	40	0.03	3×10^4	15•	744
V	259.99	−35.96	30	50–60					

Note. The kinetic temperature, radius, volume, and column density are listed for each source from Kraemer & Jackson (1999) and the electron volume density, HII mass, and stellar luminosity are from Rodriguez et al. (1982). The expansion velocities from Russeil et al. (2016; see their Table 1) are denoted by $v_{\rm ex}$. The $v_{\rm ex}$ values denoted by the • symbol are estimates based on the available $v_{\rm ex}$ of other bubbles. $B_{\rm resist}$ is the minimum magnetic field strength needed to resist the bubble's impact. These sources are associated with the WISE and Simpson bubbles.

counteract the bubble's effects, while the average field strength of the filament is ∼144 μG (Paper I). Second, we estimate the gravitational pull exerted on W6 by the two dense core hubs and find that it is 1 or 2 orders of magnitude lower than the gas or magnetic pressure of the bubble.

To calculate the gravitational pressure exerted on the bubble by the hubs, we use

$$P_{\rm grav} = \frac{GM\rho}{r}, \tag{9}$$

where G, M, ρ, and r denote the gravitational constant, the mass of each of the hub systems (to the north or south), the volume density of the bubble, and the distance between the bubble and each core-hub center, respectively. We use the virial core masses (upper estimates) from Russeil et al. (2010) to approximate the mass of each core-hub region. The sums of all cores in the northern and southern hubs are 5270 $M_\odot$ and 2124 $M_\odot$, respectively, resulting in a gravitational potential significantly less than the gas or the magnetic pressure. Even if we assume a mass of 10^4 $M_\odot$ for each hub, a distance of 2 pc from the center of the bubble, and a value of $\sim 10^3 - 10^4 \times m_p$ for ρ (where m_p is the mass of a proton), we find that gravitational pressure is 1 or 2 orders of magnitudes less than the gas or magnetic pressure. Therefore, we suggest that observed radial polarization in this region is caused by the bubble.

The center of W7 (and the shell of S7) corresponds to the center of source A, which has a magnetic field that varies across its diameter (∼200″; Sarma et al. 2000). The second-strongest maser (H_2O masers; Moran & Rodriguez 1980) in NGC 6334 and a Herbig–Haro-like object are both associated with this source, which has a bipolar structure, as illustrated in Figure 7 (due to the HII region being constrained by a dense molecular gas structure). The molecular toroid at the center of this source contains ∼2000$M_\odot$ (Sarma et al. 2000) and may serve as a nursery for the formation of a protocluster of stars (Persi et al. 2009). Our results indicate that the observed Zeeman and DCF measurements are smaller than the $B_{\rm resist}$ value that would be needed to provide support in this region by a factor of 5 (or an order of magnitude); thus, the field lines are clearly altered by the two lobes, resulting in the observed radial polarization.

W8 corresponds to the southernmost continuum source (source V; McBreen et al. 1979), which exhibits evidence for recent star formation activity (Kraemer & Jackson 1999) and is associated with H_2O and OH masers (Moran & Rodriguez 1980). This source contains a near-infrared bipolar nebula

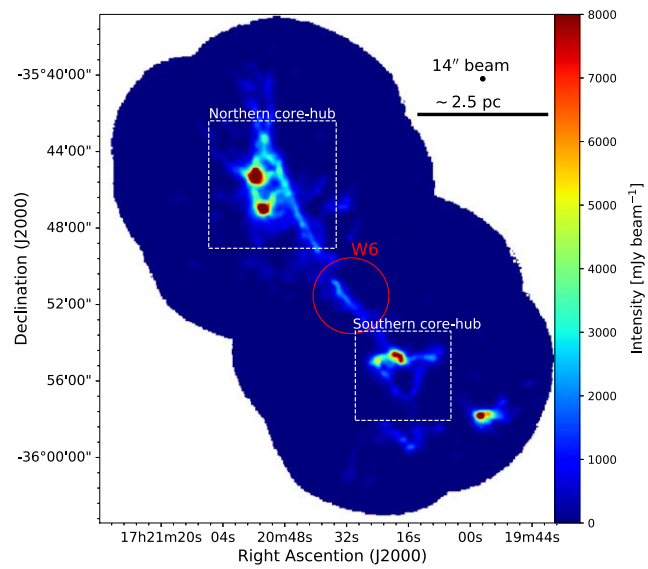

Figure 11. Two dense star-forming regions within NGC 6334, each containing a number of cores. W6 is bounded on both sides by the two core-hub systems.

(Persi 2019) and has no associated Zeeman magnetic field detections.

To summarize, the observations and analyses presented in this section strongly suggest that HII regions are responsible for the radial polarization seen in W5 (and S5), W6, W7 (and S7-a), and W8. These bubbles show evidence of radial polarization at a radius or a range of radii accompanied by increased polarization fraction, which is likely due to ordered magnetic fields. Additionally, some studies (Hoang et al. 2019; Lee et al. 2020; Tram et al. 2021) predict an increase in polarization fraction as the distance from the center of the bubble increases, which can work together with ordered field lines and result in the observed locally maximal polarization fractions.

4.1.4. Energy Balance of Individual Bubbles: Bubbles without Radial Polarization

W2 (and S2-a) and W3 (and S3) are located in a denser region of NGC 6334 and are spatially associated with sources E (S2-a) and F (S3). The magnetic field in the neighborhood of sources E and F exhibits an hourglass morphology (Zhang et al. 2014; Cortes et al. 2021). Two possible explanations for the magnetic field morphology associated with these bubbles are as follows: (1) because dust polarization observations are more

sensitive to denser regions, we may be observing plane-of-sky magnetic fields associated with the foreground or background of these HII regions, possibly accumulated on the shells; or (2) due to the higher densities in these regions, the ionized gas and outflow may lack the energy required to be dynamically important and alter the magnetic field morphology. Additionally, these two bubbles are younger and less evolved than other regions analyzed in this study. Therefore, they might not have had enough time to advance far enough into their cloud environment and reorder the field lines there.

To explore these possibilities, we estimate the background and/or foreground (i.e., non-HII) contribution to the I, Q, and U parameters in this neighborhood. To this end, we pick the interior region of S2-a that has a more coherent magnetic field morphology compared to the rest of the region (within $r \simeq 24''$) and average its Stokes I, Q, and U values. We then subtract these values from the corresponding observed values (in each pixel) and repeat the radial polarization analysis. The results are shown in Figure 12, where W2 exhibits no sign of radial polarization again, and W3 (between 30″ and 75″; and S3 outside the bubble) and S2-a (at 27″) show evidence of radial polarization.

The new (subtracted) radial polarization patterns associated with these bubbles may indicate that these bubbles have altered the field lines (first explanation). However, the observed magnetic field strengths are not small enough to confirm this. S2-a coincides with source E, and its observed Zeeman measurements (340 ± 78 with OH; Sarma et al. 2000) have a similar value as $B_{\rm resist}$ (397 μG). W3 and S3 correspond to source F, an ultracompact HII region with magnetic field strength of ~ -2000 to -5000 μG (OH Zeeman; Hunter et al. 2018). This observed field value is greater (by a factor of 2 or more) than the region's $B_{\rm resist}$ value of 744 μG. These field values indicate that the bubbles had no observable impact on the field lines due to the high density of the region (second explanation). Higher-resolution observations of these bubbles may shed light on the roles that these bubbles may have played in shaping the field lines in this region.

4.2. Machine Vision Algorithms to Identify Regions Impacting Field Lines

Using published catalogs, we identified bubbles with radial polarization in Section 3. In this section, we explore the feasibility of future studies using machine vision to identify regions with circular magnetic field morphologies (such as NGC 6334 HII regions, where the field lines are oriented tangential to the bubble boundaries). To this end, we use the circular Hough transform technique (CHT).

CHT has been applied to a number of fields, most notably industrial applications such as eye detection (e.g., Wan Mohd Khairosfaizal & Nor'aini 2009) and traffic control (e.g., Widyantoro & Saputra 2015). Edge-detection algorithms are required when applying the CHT technique. To achieve the best results, we employ Canny edge detection[97] (Canny 1986), a numerical technique developed to optimize edge derivation. The Canny edge-detection technique requires (as input) the smoothing width of the image as well as two threshold values for a double thresholding system (hysteresis thresholding), with the higher threshold typically set to be twice as high as the lower one.

Our approach includes the following two main steps, to locate regions that have pushed the magnetic field lines perpendicular to bubbles:

1. We apply the CHT on two distinct maps: one is the presence of polarization data with S/N(I)>10 and S/N (PI)>3 (hereafter referred to as PolPres map), and the other is the polarization fraction (PF map; with the same selection criteria). The PolPres map has pixel values of 0 or 1 to indicate the presence or absence of data meeting the aforementioned selection criteria. The pixel values of the PF map are not binary and influence the edge detection. Different threshold values for both PolPres and PF maps, as well as the automatic Otso threshold determination,[98] all yield results similar to the default threshold values of the Canny edge-detection library.
2. Using the circular Hough transform, we identify all possible circular patterns with radii ranging from 8″ to ∼130″, separately in each map. We then select those features that are identified in both maps at a similar location and radius (with a ∼40″ difference allowance for their center location and a one-pixel difference allowance for their radius). Because some patterns are identified multiple times, we then average the radii and locations of bubble centers that are close together (within 20″). We refer to the final selected circular features as CHT bubbles and denote them with the letter "C" followed by a number corresponding to the WISE bubbles.

In Section 3, we found that W1, W5, W6, W7, and W8 exhibit radial polarization,[99] among which W1, W5, and W7 are the only ones with polarization data covering more than ∼20% of the bubble's shell. Therefore, we propose that this technique should identify W1, W5, and W7. As proposed, we find that the technique identifies W1, W5, and W7 (denoted as C1, C5, and C7, illustrated in Figure 13). As a result, we believe the technique is promising and should be examined further with additional observations. Furthermore, the edges of W6 and S7-a (corresponding to C6 and C7-a) and an additional circular feature, C0, are identified in this technique. C6 coincides with the southern edge of W6 (a subregion with clear radial polarization pattern), and C7-a overlaps with the northeastern side of S7-a.

The magnetic fields associated with C0 exhibit a radial polarization morphology between ∼45″ and 53″ (see Figure 14). Because this region overlaps with W4, we suggest that C0 may be a distinct HII region that was previously undetected due to line-of-sight confusion with W4. These findings indicate that while the CHT technique is used in a basic and simple form here, it has significant potential for detecting bubbles that have altered the magnetic field lines. These regions may be detected in full sky observations using more complex CHT techniques (e.g., Yadav et al. 2014) and/or machine learning.

4.3. Cloud and Magnetic Field Coevolution

The large-scale $B_{\rm POS}$ lines are predominantly perpendicular to the main ridge of NGC 6334 (Li et al. 2015), which are

[97] We use the already-existing edge-detection class in the Skit-image Python library (van der Walt et al. 2014).

[98] skimage.filters.threshold_otsu.

[99] W2, S2-a, W3, and S3 do not exhibit radial polarization in the observations.

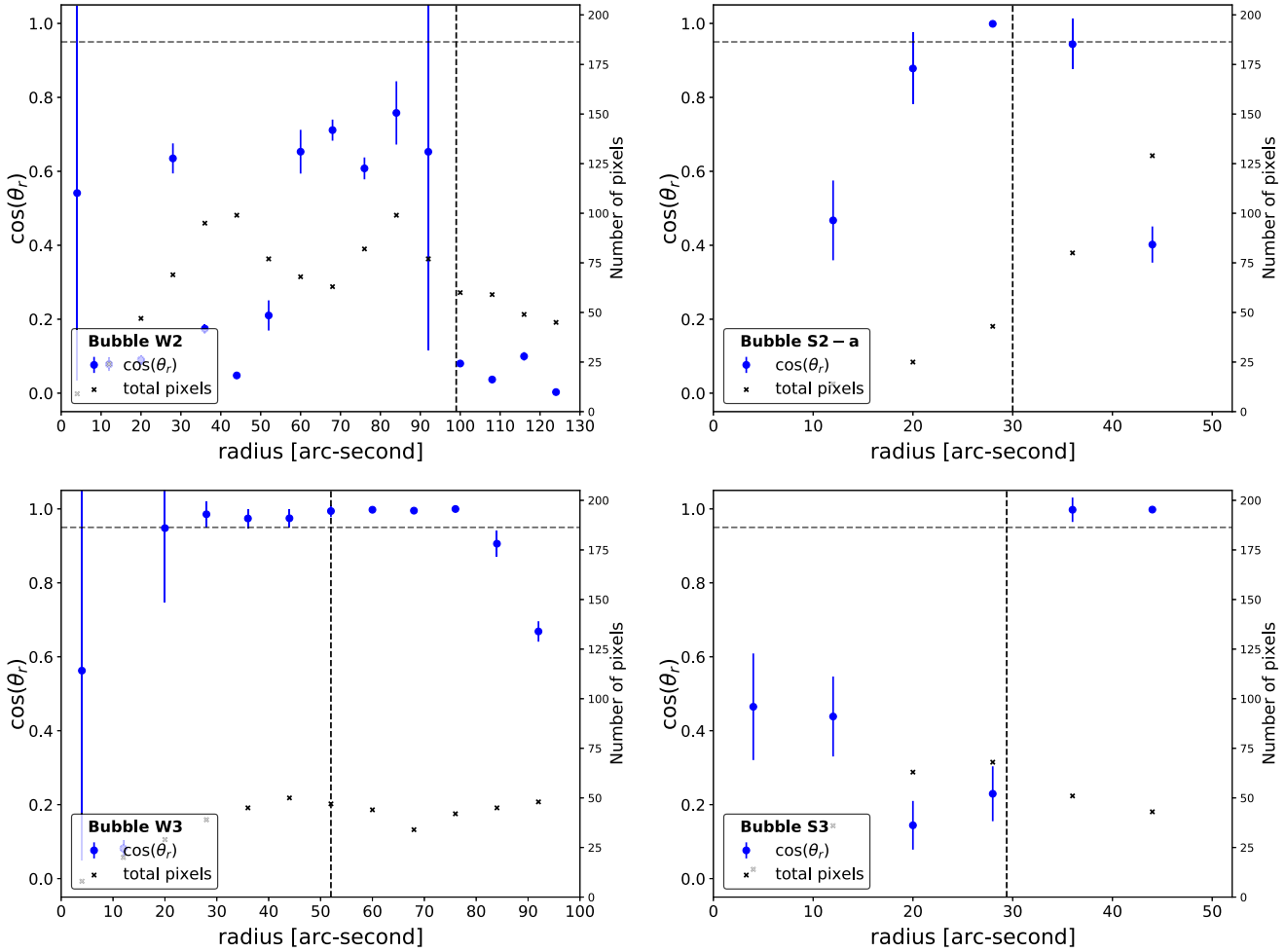

Figure 12. Radial polarization analysis with non-HII effects subtracted for W2, S2-a, W3, and S3. The vertical dashed line shows each bubble's radius identified by the WISE and Simpson catalogs. The black markers indicate the number of pixels contained in each annulus. The blue points represent $\cos\theta_r$. In these plots, evidence of radial polarization is present at 27″ for S2-a, between ∼33″ and 45″ for W3, and beyond 25″ for S3.

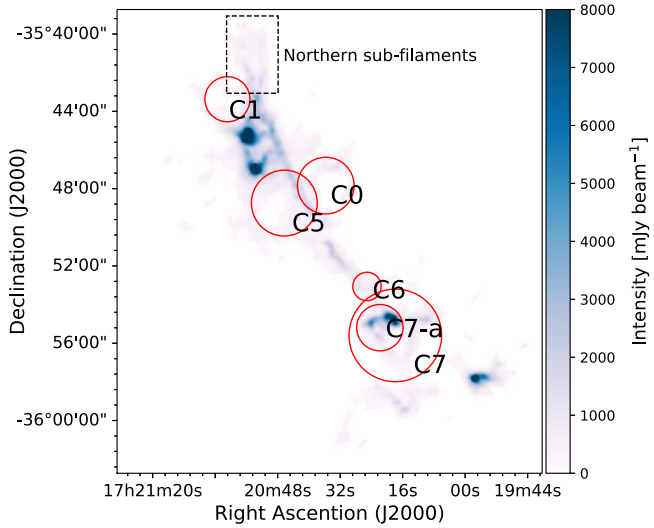

Figure 13. Identified bubbles using circular Hough transform (CHT). We identify bubbles that have altered the magnetic field lines. Some bubbles are identified multiple times, which are then averaged to one. The dashed black rectangle indicates the location of the two merging subfilaments discussed in Paper I.

altered on substructure scales by HII regions within the cloud. We suggest that these $B_{\rm POS}$ lines were initially even more coherent and perpendicular to the filament, but were then altered by feedback mechanisms, such as HII regions, or gas flows (see the filament within W6), as illustrated in a schematic view by Figure 15.

Additionally, the physical properties of HII regions may reveal the initial orientation of the magnetic field prior to the HII expansion. For instance, studies (e.g., Chen et al. 2022) indicate that HII regions may be elongated along the initial orientation of the field lines as expansion perpendicular to the field lines is met with resistance. Bonne et al. (2022) suggested that the initial magnetic field orientation may have also enforced the orientation of bipolar cavities in the Vela C cloud. We note that the elliptical elongations of the NGC 6334 bubbles are reported in the MIR observations of Simpson et al. (2012), but they are very small, except for S2-a, as illustrated in Figure 16 where the elongation of the bubble is not completely aligned with the large-scale magnetic fields (Chen et al. 2022).

The overall perpendicular $B_{\rm POS}$ lines to the main ridge (particularly at earlier evolutionary stages of the cloud) and the presence of large bubbles in this region, such as W5, may

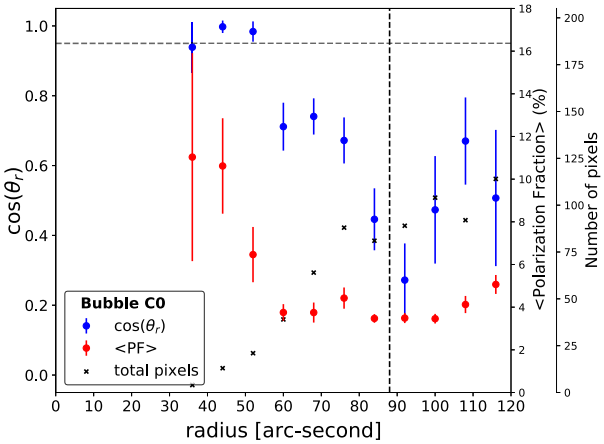

Figure 14. Radial polarization analysis of C0. The mean polarization fraction, the total number of pixels in each shell (which satisfy the selection criteria of S/N(I)>10 and S/N(PI)>3), and cos(θ_r) are all shown by the red, black, and blue markers.

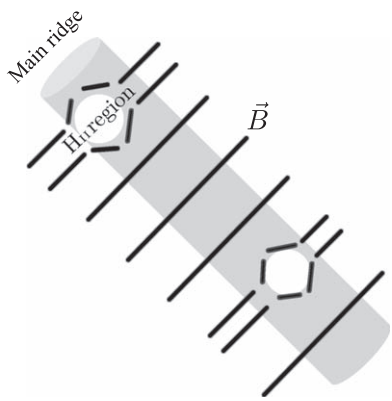

Figure 15. A schematic illustration of perpendicular $B_{\rm POS}$ field lines on a dense molecular cloud with HII region influences. We propose that the plane-of-sky magnetic field lines in NGC 6334 are generally perpendicular to the main ridge and that the nonperpendicular lines are due to impacts by HII regions or the gas flow (filament within W6). The cloud (or main ridge), magnetic field lines, and HII regions are depicted by a cylinder, black lines, and circular cavities, respectively.

indicate that NGC 6334 formed via a cloud–cloud collision (Inoue & Fukui 2013; Fukui et al. 2018, 2021; Hayashi et al. 2021) or a shock–cloud interaction (Inutsuka et al. 2015; Inoue et al. 2018; Abe et al. 2021). These cloud-formation models often result in an arc-shaped (bow-shaped) magnetic field morphology (Heiles 1997; Tahani et al. 2019, 2022a, 2022b) that may appear perpendicular to the cloud when projected onto the plane of the sky. The shock–cloud interaction model is also supported in other regions by line-of-sight (Tahani et al. 2018, 2020) and 3D (Tahani et al. 2019, 2022a, 2022b; Tahani 2022) magnetic field and velocity (Arzoumanian et al. 2018; Bonne et al. 2020) observations.

5. Summary and Conclusion

We investigated the magnetic field morphology of HII regions associated with NGC 6334, using the JCMT BISTRO 850 μm dust polarization observations. We located these bubbles using the WISE (Anderson et al. 2014) and Simpson et al. (2012) catalogs and studied the presence of radial polarization patterns in each bubble by transforming the reference frame of the observations with respect to the bubble. This enabled us to identify bubbles that had altered their surrounding magnetic field morphology. Additionally, we compared the gas and magnetic pressures within each bubble using previously determined Zeeman magnetic field strengths in order to bolster our conclusion regarding the magnetic field morphologies associated with these bubbles.

We found evidence of radial polarization associated with W1, W5 (or S5), W6, W7 (or S7-a), and W8. The radial polarization is prominent in W5 (or S5) and W6, weak in W1 and S7-a, and absent in W2. S2-a and W3 (and S3) may indicate radial polarization after subtracting the non-HII contributions. We propose that the magnetic field morphology of the NGC 6334 cloud was originally coherent and perpendicular to the cloud, but was altered during cloud evolution as a result of internal feedback mechanisms or gas flow.

We found that the presence or indication of radial polarization (tangential field lines) associated with HII regions is accompanied by a higher polarization fraction. Quantifying the relationship between polarization fraction and bubble physical properties requires a statistical analysis of a large number of bubbles and should be investigated in subsequent studies.

We found a bipolar polarization structure associated with W7, characterized by a clear radial polarization pattern for its northern lobe. To our knowledge, this is the first time that polarization data have been used to identify bubbles (or lobes within HII regions). To take this a step further, we applied a computer vision approach based on the circular Hough transform on the dust polarization observations to identify and recognize bubbles that had altered their surrounding magnetic morphology. A more advanced computer vision or machine-learning algorithm can enhance this technique, allowing it to be applied to additional regions or the entire sky.

This program is part of the JCMT BISTRO Large Program observed under project code M17BL011. Team BISTRO-J is in part financially supported by 260 individuals. The James Clerk Maxwell Telescope is operated by the East Asian Observatory on behalf of the National Astronomical Observatory of Japan; Academia Sinica Institute of Astronomy and Astrophysics; the Korea Astronomy and Space Science Institute; Center for Astronomical Mega-Science (as well as the National Key R&D Program of China with No. 2017YFA0402700). Additional funding support is provided by the Science and Technology Facilities Council of the United Kingdom and participating universities in the United Kingdom, Canada, and Ireland. Additional funds for the construction of SCUBA-2 and POL-2 were provided by the Canada Foundation for Innovation.

The authors wish to recognize and acknowledge the very significant cultural role and reverence that the summit of Maunakea has always had within the indigenous Hawaiian community. We are most fortunate to have the opportunity to conduct observations from this mountain.

We used LATEX, Python and its associated libraries including astropy (Astropy Collaboration et al. 2013), PyCharm, Jupyter notebook, SAO Image DS9, and the Starlink (Currie et al. 2014) software. QuillBot[100] was employed to edit the text.

M.T. is supported by the Banting Fellowship (Natural Sciences and Engineering Research Council Canada) hosted at

[100] https://quillbot.com/

Stanford University and the Kavli Institute for Particle Astrophysics and Cosmology (KIPAC) Fellowship. K.P. is a Royal Society University Research Fellow, supported by Grant No. URF\R1\211322.

D.J. is supported by the National Research Council of Canada and by a Natural Sciences and Engineering Research Council Discovery grant. Y.D. is supported by JSPS KAKENHI grants 25247016 and 18H01250. T.O. acknowledges a Grant-in-Aid for Scientific Research of JSPS (18K03691). Mo.Ta. is supported by JSPS KAKENHI grant Nos. 18H05442, 15H02063, and 22000005. J.K. is supported by JSPS KAKENHI grant No. 19K14775. W.K. is supported by the National Research Foundation of Korea (NRF) grant funded by the Korea government (MSIT) (NRF-2021R1F1A1061794). F.P. acknowledges support from the Spanish State Research Agency (AEI) under grant No. PID2019-105552RB-C43, and support from the Agencia Canaria de Investigación, Innovación y Sociedad de la Información (ACIISI) under the European FEDER (FONDO EUROPEO DE DESARROLLO REGIONAL) de Canarias 2014-2020 grant No. PROID2021010078. C.E. acknowledges the financial support from grant RJF/2020/000071 as a part of the Ramanujan Fellowship awarded by the Science and Engineering Research Board (SERB), Department of Science and Technology (DST), Government of India. L.F. acknowledges support from the Ministry of Science and Technology of Taiwan, under grant Nos. MoST107-2119-M-001-031- MY3, 111-2811-M-005-007, and 109-2112-M-005-003-MY3, and from Academia Sinica under grant No. AS-IA-106-M03. F.K. is supported by the Spanish program Unidad de Excelencia María de Maeztu CEX2020-001058-M, financed by MCIN/AEI/10.13039/501100011033. C.W.L. is supported by the Basic Science Research Program through the National Research Foundation of Korea (NRF) funded by the Ministry of Education, Science and Technology(NRF-2019R1A2C1010851), and by the Korea Astronomy and Space Science Institute grant funded by the Korea government (MSIT) (Project No. 2022-1-840-05). SPL acknowledges the grant from the National Science and Technology Council of Taiwan 109-2112-M-007-010-MY3.

Appendix A
Error Bars

To determine the error bars associated with $\cos(\theta_r)$, we use the following error propagation equation:

$$\delta f = \sqrt{\left(\frac{\partial f}{\partial Q_r}\right)^2 (\delta Q_r)^2 + \left(\frac{\partial f}{\partial U_r}\right)^2 (\delta U_r)^2}\,, \tag{A1}$$

where δQ_r and δU_r represent the standard deviation of the mean of $\langle Q_r\rangle$ and $\langle U_r\rangle$ of each annulus, respectively, and

$$\begin{aligned} f &= \cos\theta_r, \\ \theta_r &= 0.5 \times \arctan(\langle U_r\rangle, \langle Q_r\rangle), \\ \frac{\partial f}{\partial U_r} &= -0.5 \times \sin\theta_r \times \frac{1}{\langle Q_r\rangle\left(1 + \left(\frac{\langle U_r\rangle}{\langle Q_r\rangle}\right)^2\right)}, \\ \frac{\partial f}{\partial Q_r} &= 0.5 \times \sin\theta_r \times \frac{1}{1 + \left(\frac{\langle U_r\rangle}{\langle Q_r\rangle}\right)^2}, \times \frac{\langle U_r\rangle}{\langle Q_r\rangle^2}. \end{aligned} \tag{A2}$$

Appendix B
Elliptical Bubble

The bubbles in the Simpson et al. (2012) catalog are initially classified as ellipses. The Simpson catalog includes inner and outer radii for both the X- and Y-directions, as well as their eccentricity values, as illustrated in Figure 16. We examined the radial polarization patterns of these regions and found that they were very similar to the results presented in Figures 7 and 8, due to the small eccentricity values of these bubbles.

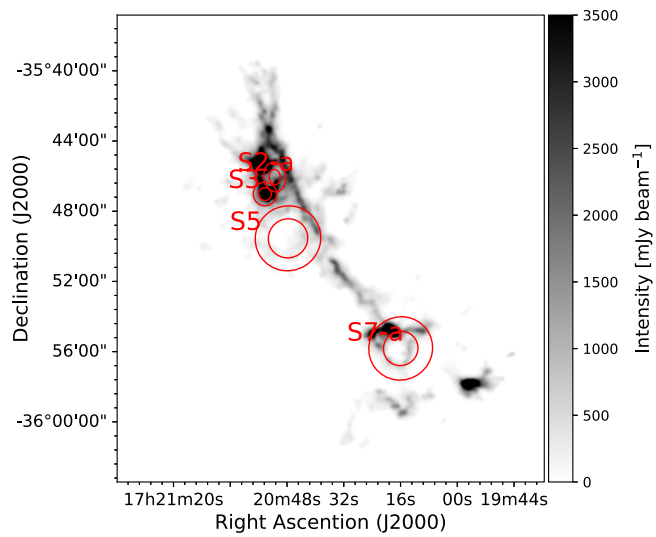

Figure 16. The Simpson bubbles illustrated in their elliptical form. The numbers show the Simpson bubbles specified in Figure 3. The inner and outer radii corresponding to each bubble are illustrated with red ellipses.

ORCID iDs

Mehrnoosh Tahani https://orcid.org/0000-0001-8749-1436
Pierre Bastien https://orcid.org/0000-0002-0794-3859
Ray S. Furuya https://orcid.org/0000-0003-0646-8782
Kate Pattle https://orcid.org/0000-0002-8557-3582
Doug Johnstone https://orcid.org/0000-0002-6773-459X
Doris Arzoumanian https://orcid.org/0000-0002-1959-7201
Yasuo Doi https://orcid.org/0000-0001-8746-6548
Tetsuo Hasegawa https://orcid.org/0000-0003-1853-0184
Shu-ichiro Inutsuka https://orcid.org/0000-0003-4366-6518
Simon Coudé https://orcid.org/0000-0002-0859-0805
Laura Fissel https://orcid.org/0000-0002-0859-0805
Michael Chun-Yuan Chen https://orcid.org/0000-0003-4242-973X
Frédérick Poidevin https://orcid.org/0000-0002-5391-5568
Sarah Sadavoy https://orcid.org/0000-0001-7474-6874
Rachel Friesen https://orcid.org/0000-0001-7594-8128
Patrick M. Koch https://orcid.org/0000-0003-2777-5861
James Di Francesco https://orcid.org/0000-0002-9289-2450
Gerald H. Moriarty-Schieven https://orcid.org/0000-0002-0393-7822
Zhiwei Chen https://orcid.org/0000-0003-0849-0692
Eun Jung Chung https://orcid.org/0000-0003-0014-1527
Chakali Eswaraiah https://orcid.org/0000-0003-4761-6139
Lapo Fanciullo https://orcid.org/0000-0001-9930-9240
Tim Gledhill https://orcid.org/0000-0002-2859-4600
Valentin J. M. Le Gouellec https://orcid.org/0000-0002-5714-799X

Thiem Hoang https://orcid.org/0000-0003-2017-0982
Jihye Hwang https://orcid.org/0000-0001-7866-2686
Ji-hyun Kang https://orcid.org/0000-0001-7379-6263
Kyoung Hee Kim https://orcid.org/0000-0001-9597-7196
Florian Kirchschlager https://orcid.org/0000-0002-3036-0184
Woojin Kwon https://orcid.org/0000-0003-4022-4132
Chang Won Lee https://orcid.org/0000-0002-3179-6334
Hong-Li Liu https://orcid.org/0000-0003-3343-9645
Takashi Onaka https://orcid.org/0000-0002-8234-6747
Mark G. Rawlings https://orcid.org/0000-0002-6529-202X
Archana Soam https://orcid.org/0000-0002-6386-2906
Motohide Tamura https://orcid.org/0000-0002-6510-0681
Xindi Tang https://orcid.org/0000-0002-4154-4309
Kohji Tomisaka https://orcid.org/0000-0003-2726-0892
Jungmi Kwon https://orcid.org/0000-0003-2815-7774
Thuong D. Hoang https://orcid.org/0000-0002-3437-5228
Matt Redman https://orcid.org/0000-0002-1021-9343
David Berry https://orcid.org/0000-0001-6524-2447
Tao-Chung Ching https://orcid.org/0000-0001-8516-2532
Jia-Wei Wang https://orcid.org/0000-0002-6668-974X
Shih-Ping Lai https://orcid.org/0000-0001-5522-486X
Keping Qiu https://orcid.org/0000-0002-5093-5088
Derek Ward-Thompson https://orcid.org/0000-0003-1140-2761
Martin Houde https://orcid.org/0000-0003-4420-8674
Do-Young Byun https://orcid.org/0000-0003-1157-4109
Huei-Ru Vivien Chen https://orcid.org/0000-0002-9774-1846
Wen Ping Chen https://orcid.org/0000-0003-0262-272X
Jungyeon Cho https://orcid.org/0000-0003-1725-4376
Antonio Chrysostomou https://orcid.org/0000-0002-9583-8644
Pham Ngoc Diep https://orcid.org/0000-0002-2808-0888
Hao-Yuan Duan https://orcid.org/0000-0002-7022-4742
Erica Franzmann https://orcid.org/0000-0003-2142-0357
Per Friberg https://orcid.org/0000-0002-8010-8454
Gary Fuller https://orcid.org/0000-0001-8509-1818
Sarah F. Graves https://orcid.org/0000-0001-9361-5781
Jane S. Greaves https://orcid.org/0000-0002-3133-413X
Qilao Gu https://orcid.org/0000-0002-2826-1902
Jennifer Hatchell https://orcid.org/0000-0002-4870-2760
Saeko S. Hayashi https://orcid.org/0000-0001-5026-490X
Charles L. H. Hull https://orcid.org/0000-0002-8975-7573
Tsuyoshi Inoue https://orcid.org/0000-0002-7935-8771
Il-Gyo Jeong https://orcid.org/0000-0002-5492-6832
Miju Kang https://orcid.org/0000-0002-5016-050X
Sung-ju Kang https://orcid.org/0000-0002-5004-7216
Akimasa Kataoka https://orcid.org/0000-0003-4562-4119
Koji S. Kawabata https://orcid.org/0000-0001-6099-9539
Francisca Kemper https://orcid.org/0000-0003-2743-8240
Gwanjeong Kim https://orcid.org/0000-0003-2011-8172
Jongsoo Kim https://orcid.org/0000-0002-1229-0426
Kee-Tae Kim https://orcid.org/0000-0003-2412-7092
Mi-Ryang Kim https://orcid.org/0000-0002-1408-7747
Shinyoung Kim https://orcid.org/0000-0001-9333-5608
Jason M. Kirk https://orcid.org/0000-0002-4552-7477
Masato I. N. Kobayashi https://orcid.org/0000-0003-3990-1204
Vera Konyves https://orcid.org/0000-0002-3746-1498
Kevin Lacaille https://orcid.org/0000-0001-9870-5663
Chi-Yan Law https://orcid.org/0000-0003-1964-970X
Chin-Fei Lee https://orcid.org/0000-0002-3024-5864
Jeong-Eun Lee https://orcid.org/0000-0003-3119-2087
Sang-Sung Lee https://orcid.org/0000-0002-6269-594X
Yong-Hee Lee https://orcid.org/0000-0001-6047-701X
Di Li https://orcid.org/0000-0003-3010-7661
Hua-bai Li https://orcid.org/0000-0003-2641-9240
Junhao Liu https://orcid.org/0000-0002-4774-2998
Sheng-Yuan Liu https://orcid.org/0000-0003-4603-7119
Tie Liu https://orcid.org/0000-0002-5286-2564
A-Ran Lyo https://orcid.org/0000-0002-9907-8427
Steve Mairs https://orcid.org/0000-0002-6956-0730
Masafumi Matsumura https://orcid.org/0000-0002-6906-0103
Brenda C. Matthews https://orcid.org/0000-0003-3017-9577
Tetsuya Nagata https://orcid.org/0000-0001-9264-9015
Fumitaka Nakamura https://orcid.org/0000-0001-5431-2294
Nagayoshi Ohashi https://orcid.org/0000-0003-0998-5064
Geumsook Park https://orcid.org/0000-0001-8467-3736
Harriet Parsons https://orcid.org/0000-0002-6327-3423
Tae-Soo Pyo https://orcid.org/0000-0002-3273-0804
Lei Qian https://orcid.org/0000-0003-0597-0957
Ramprasad Rao https://orcid.org/0000-0002-1407-7944
John Richer https://orcid.org/0000-0002-9693-6860
Andrew Rigby https://orcid.org/0000-0002-3351-2200
Giorgio Savini https://orcid.org/0000-0003-4449-9416
Anna M. M. Scaife https://orcid.org/0000-0002-5364-2301
Hiroko Shinnaga https://orcid.org/0000-0001-9407-6775
Ya-Wen Tang https://orcid.org/0000-0002-0675-276X
Yusuke Tsukamoto https://orcid.org/0000-0001-6738-676X
Serena Viti https://orcid.org/0000-0001-8504-8844
Hongchi Wang https://orcid.org/0000-0003-0746-7968
Hsi-Wei Yen https://orcid.org/0000-0003-1412-893X
Hyunju Yoo https://orcid.org/0000-0002-8578-1728
Jinghua Yuan https://orcid.org/0000-0001-8060-3538
Hyeong-Sik Yun https://orcid.org/0000-0001-6842-1555
Chuan-Peng Zhang https://orcid.org/0000-0002-4428-3183
Yapeng Zhang https://orcid.org/0000-0002-5102-2096
Jianjun Zhou https://orcid.org/0000-0003-0356-818X
Philippe André https://orcid.org/0000-0002-3413-2293
Stewart P. S. Eyres https://orcid.org/0000-0002-6663-7675
Sam Falle https://orcid.org/0000-0002-9829-0426
Sven van Loo https://orcid.org/0000-0003-4746-8500
Jean-François Robitaille https://orcid.org/0000-0001-5079-8573

References

Abe, D., Inoue, T., Inutsuka, S.-i., & Matsumoto, T. 2021, ApJ, 916, 83
Anderson, L. D., Armentrout, W. P., Johnstone, B. M., et al. 2015, ApJS, 221, 26
Anderson, L. D., Armentrout, W. P., Luisi, M., et al. 2018, ApJS, 234, 33
Anderson, L. D., Bania, T. M., Balser, D. S., et al. 2014, ApJS, 212, 1
Anderson, L. D., Bania, T. M., Balser, D. S., & Rood, R. T. 2011, ApJS, 194, 32
Andersson, B.-G., Lazarian, A., & Vaillancourt, J. E. 2015, ARA&A, 53, 501
André, P., Revéret, V., Könyves, V., et al. 2016, A&A, 592, A54
Arthur, S. J., Henney, W. J., Mellema, G., De Colle, F., & Vazquez-Semadeni, E. 2011, MNRAS, 414, 1747
Arzoumanian, D., Furuya, R. S., Hasegawa, T., et al. 2021, A&A, 647, A78, Paper I
Arzoumanian, D., Shimajiri, Y., Inutsuka, S.-i., Inoue, T., & Tachihara, K. 2018, PASJ, 70, 96

Astropy Collaboration, Robitaille, T. P., Tollerud, E. J., et al. 2013, A&A, 558, A33
Bachiller, R., & Cernicharo, J. 1990, A&A, 239, 276
Balser, D. S., Roshi, D. A., Jeyakumar, S., et al. 2016, ApJ, 816, 22
Bania, T. M., Anderson, L. D., Balser, D. S., & Rood, R. T. 2010, ApJL, 718, L106
Bastien, P., Bissonnette, E., Simon, A., et al. 2011, in ASP Conf. Ser. 449, Astronomical Polarimetry 2008: Science from Small to Large Telescopes, ed. P. Bastien et al. (San Francisco, CA: ASP), 68
Batrla, W., Matthews, H. E., Menten, K. M., & Walmsley, C. M. 1987, Natur, 326, 49
Bohigas, J. 1992, RMxAA, 24, 121
Bonne, L., Bontemps, S., Schneider, N., et al. 2020, A&A, 644, A27
Bonne, L., Schneider, N., García, P., et al. 2022, ApJ, 935, 171
Boulares, A., & Cox, D. P. 1990, ApJ, 365, 544
Busquet, G. 2020, NatAs, 4, 1126
Cabral, B., & Leedom, L. C. 1993, in Proc. 20th Annual Conf. Computer Graphics and Interactive Techniques, SIGGRAPH '93 (New York, NY: Association for Computing Machinery), 263
Canny, J. 1986, ITPAM, 8, 679, PAMI-8
Canovas, H., Ménard, F., de Boer, J., et al. 2015, A&A, 582, L7
Caswell, J. L., & Haynes, R. F. 1987, A&A, 171, 261
Chandrasekhar, S., & Fermi, E. 1953, ApJ, 118, 113
Chen, Z., Jiang, Z., Tamura, M., Kwon, J., & Roman-Lopes, A. 2017, ApJ, 838, 80
Chen, Z., Jiang, Z., Wang, Y., et al. 2012, PASJ, 64, 110
Chen, Z., Sefako, R., Yang, Y., et al. 2022, RAA, 22, 075017
Chung, E. J., Lee, C. W., Kwon, W., et al. 2022, AJ, 164, 175
Comeron, F. 1997, A&A, 326, 1195
Cortes, P. C., Sanhueza, P., Houde, M., et al. 2021, ApJ, 923, 204
Currie, M. J., Berry, D. S., Jenness, T., et al. 2014, in ASP Conf. Ser. 485, Astronomical Data Analysis Software and Systems XXIII, ed. N. Manset & P. Forshay (San Francisco, CA: ASP), 391
Davis, L., Jr., & Greenstein, J. L. 1951, ApJ, 114, 206
Deharveng, L., Zavagno, A., & Caplan, J. 2005, A&A, 433, 565
Devaraj, R., Clemens, D. P., Dewangan, L. K., et al. 2021, ApJ, 911, 81
Dewangan, L. K., Devaraj, R., & Ojha, D. K. 2018, ApJ, 854, 106
Doi, Y., Hasegawa, T., Furuya, R. S., et al. 2020, ApJ, 899, 28
Draine, B. T. 2009, in ASP Conf. Ser. 414, Cosmic Dust—Near and Far, ed. T. Henning, E. Grün, & J. Steinacker (San Francisco, CA: ASP), 453
Draine, B. T., & Weingartner, J. C. 1997, ApJ, 480, 633
Elmegreen, B. G. 1998, in ASP Conf. Ser. 148, Origins, ed. C. E. Woodward et al. (San Francisco, CA: ASP), 150
Eswaraiah, C., Lai, S.-P., Chen, W.-P., et al. 2017, ApJ, 850, 195
Eswaraiah, C., Li, D., Samal, M. R., et al. 2020, ApJ, 897, 90
Federrath, C. 2015, MNRAS, 450, 4035
Fernández-López, M., Sanhueza, P., Zapata, L. A., et al. 2021, ApJ, 913, 29
Fissel, L. M., Ade, P. A. R., Angilè, F. E., et al. 2016, ApJ, 824, 134
Forster, J. R., & Caswell, J. L. 1989, A&A, 213, 339
Friberg, P., Bastien, P., Berry, D., et al. 2016, Proc. SPIE, 9914, 991403
Fukui, Y., Habe, A., Inoue, T., Enokiya, R., & Tachihara, K. 2021, PASJ, 73, S1
Fukui, Y., Kohno, M., Yokoyama, K., et al. 2018, PASJ, 70, S41
Gum, C. S. 1955, MmRAS, 67, 155
Harvey, P. M., & Gatley, I. 1983, ApJ, 269, 613
Hayashi, K., Yoshiike, S., Enokiya, R., et al. 2021, PASJ, 73, S321
Heiles, C. 1997, ApJS, 111, 245
Henney, W. J., Arthur, S. J., De Colle, F., & Mellema, G. 2009, MNRAS, 398, 157
Hoang, T., & Lazarian, A. 2016, ApJ, 831, 159
Hoang, T., Tram, L. N., Lee, H., & Ahn, S.-H. 2019, NatAs, 3, 766
Hoang, T. D., Ngoc, N. B., Diep, P. N., et al. 2022, ApJ, 929, 27
Holland, W. S., Bintley, D., Chapin, E. L., et al. 2013, MNRAS, 430, 2513
Hull, C. L. H., & Plambeck, R. L. 2015, JAI, 4, 1550005
Hunter, T. R., Brogan, C. L., MacLeod, G. C., et al. 2018, ApJ, 854, 170
Inoue, T., & Fukui, Y. 2013, ApJL, 774, L31
Inoue, T., Hennebelle, P., Fukui, Y., et al. 2018, PASJ, 70, S53
Inutsuka, S.-i., Inoue, T., Iwasaki, K., & Hosokawa, T. 2015, A&A, 580, A49
Koch, P. M., Tang, Y.-W., & Ho, P. T. P. 2012a, ApJ, 747, 79
Koch, P. M., Tang, Y.-W., & Ho, P. T. P. 2012b, ApJ, 747, 80
Könyves, V., Ward-Thompson, D., Pattle, K., et al. 2021, ApJ, 913, 57
Kraemer, K. E., & Jackson, J. M. 1999, ApJS, 124, 439
Krumholz, M. R., & Federrath, C. 2019, FrASS, 6, 7
Krumholz, M. R., Stone, J. M., & Gardiner, T. A. 2007, ApJ, 671, 518
Lazarian, A. 2007, J. Quant. Spec. Radiat. Transf., 106, 225
Lazarian, A., & Hoang, T. 2007, MNRAS, 378, 910
Lee, H., Hoang, T., Le, N., & Cho, J. 2020, ApJ, 896, 44
Li, P. S., McKee, C. F., & Klein, R. I. 2015, MNRAS, 452, 2500
Liu, T., Li, P. S., Juvela, M., et al. 2018, ApJ, 859, 151
Loughran, L., McBreen, B., Fazio, G. G., et al. 1986, ApJ, 303, 629
McBreen, B., Fazio, G. G., Stier, M., & Wright, E. L. 1979, ApJL, 232 L183
Menten, K. M., & Batrla, W. 1989, ApJ, 341, 839
Montier, L., Plaszczynski, S., Levrier, F., et al. 2015, A&A, 574, A136
Moran, J. M., & Rodriguez, L. F. 1980, ApJL, 236, L159
Nakamura, F., & Li, Z.-Y. 2007, ApJ, 662, 395
Neckel, T. 1978, A&A, 69, 51
Ntormousi, E., Dawson, J. R., Hennebelle, P., & Fierlinger, K. 2017, A&A, 599, A94
Offner, S. S. R., & Liu, Y. 2018, NatAs, 2, 896
Osterbrock, D. E., & Ferland, G. J. 2006, Astrophysics of Gaseous Nebulae and Active Galactic Nuclei (Sausalito, CA: University Science Books)
Pattle, K., & Fissel, L. 2019, FrASS, 6, 15
Pattle, K., Fissel, L., Tahani, M., Liu, T., & Ntormousi, E. 2022, arXiv:2203.11179
Pattle, K., Lai, S.-P., Hasegawa, T., et al. 2019, ApJ, 880, 27
Pattle, K., Lai, S.-P., Di Francesco, J., et al. 2021, ApJ, 907, 88
Pattle, K., Ward-Thompson, D., Hasegawa, T., et al. 2018, ApJL, 860, L6
Pavel, M. D., & Clemens, D. P. 2012, ApJ, 760, 150
Pereyra, A., & Magalh aes, A. M. 2007, ApJ, 662, 1014
Persi, P. 2019, in Frontier Research in Astrophysics—III (Trieste: PoS), 29
Persi, P., & Tapia, M. 2008, in Star Formation in NGC 6334, ed. B. Reipurth, Vol. 5 (San Francisco, CA: ASP), 456
Persi, P., Tapia, M., Roth, M., & Gomez, M. 2009, A&A, 493, 571
Pillai, T. G. S., Clemens, D. P., Reissl, S., et al. 2020, NatAs, 4, 1195
Plaszczynski, S., Montier, L., Levrier, F., & Tristram, M. 2014, MNRAS, 439, 4048
Quireza, C., Rood, R. T., Balser, D. S., & Bania, T. M. 2006, ApJS, 165 338
Reissl, S., Klessen, R. S., Mac Low, M.-M., & Pellegrini, E. W. 2018, A&A, 611, A70
Rodriguez, L. F., Canto, J., & Moran, J. M. 1982, ApJ, 255, 103
Rodriguez, L. F., Canto, J., & Moran, J. M. 1988, ApJ, 333, 801
Rodríguez, L. F., Masqué, J. M., Dzib, S. A., Loinard, L., & Kurtz, S. E. 2014, RMxAA, 50, 3
Russeil, D., Zavagno, A., Motte, F., et al. 2010, A&A, 515, A55
Russeil, D., Zavagno, A., Adami, C., et al. 2012, A&A, 538, A142
Russeil, D., Tige, J., Adami, C., et al. 2016, A&A, 587, A135
Sadaghiani, M., Sánchez-Monge, Á, Schilke, P., et al. 2020, A&A, 635, A2
Santos, F. P., Franco, G. A. P., Roman-Lopes, A., Reis, W., & Román-Zúniga, C. G. 2014, ApJ, 783, 1
Sarma, A. P., Troland, T. H., Roberts, D. A., & Crutcher, R. M. 2000, ApJ, 533, 271
Schmid, H. M., Joos, F., & Tschan, D. 2006, A&A, 452, 657
Schneider, N., Simon, R., Guevara, C., et al. 2020, PASP, 132, 104301
Serkowski, K. 1962, AdA&A, 1, 289
Shimajiri, Y., Andre, P., Ntormousi, E., et al. 2019, A&A, 632, A83
Simpson, R. J., Povich, M. S., Kendrew, S., et al. 2012, MNRAS, 424, 2442
Soam, A., Maheswar, G., Lee, C. W., Neha, S., & Andersson, B. G. 2017, MNRAS, 465, 559
Soam, A., Maheswar, G., Lee, C. W., Neha, S., & Kim, K.-T. 2018, MNRAS, 476, 4782
Straw, S. M., Hyland, A. R., & McGregor, P. J. 1989, ApJS, 69, 99
Tahani, M. 2022, FrASS, 9, 940027
Tahani, M., Plume, R., & Brown, J. 2020, in Proc. of the IAU, Astronomy in Focus XXX (Cambridge: Cambridge Univ. Press), 103
Tahani, M., Lupypciw, W., Glover, J., et al. 2022b, A&A, 660, A97
Tahani, M., Glover, J., Lupypciw, W., et al. 2022a, A&A, 660, L7
Tahani, M., Plume, R., Brown, J. C., & Kainulainen, J. 2018, A&A, 614 A100
Tahani, M., Plume, R., Brown, J. C., Soler, J. D., & Kainulainen, J. 2019, A&A, 632, A68
Tang, Y.-W., Ho, P. T. P., Girart, J. M., et al. 2009, ApJ, 695, 1399
Tapia, M., Persi, P., & Roth, M. 1996, A&A, 316, 102
Thompson, M. A., Urquhart, J. S., Moore, T. J. T., & Morgan, L. K. 2012, MNRAS, 421, 408
Tram, L. N., Hoang, T., Lee, H., et al. 2021, ApJ, 906, 115
Tremblin, P., Audit, E., Minier, V., Schmidt, W., & Schneider, N. 2012, A&A, 546, A33
Vaillancourt, J. 2006, PASP, 118, 1340

van der Walt, S., Schonberger, J. L., Nunez-Iglesias, J., et al. 2014, PeerJ, 2, e453
Wan Mohd Khairosfaizal, W. M. K., & Nor'aini, A. J. 2009, in 2009 5th Int. Colloquium on Signal Processing Its Applications (Piscataway, NJ: IEEE), 238
Wang, P., Li, Z.-Y., Abel, T., & Nakamura, F. 2010, ApJ, 709, 27
Ward-Thompson, D., Pattle, K., Bastien, P., et al. 2017, ApJ, 842, 66
Wardle, J. F. C., & Kronberg, P. P. 1974, ApJ, 194, 249
Widyantoro, D. H., & Saputra, K. I. 2015, in 2015 Int. Conf. Data and Software Engineering (ICoDSE) (Piscataway, NJ: IEEE), 237
Wu, Y. W., Sato, M., Reid, M. J., et al. 2014, A&A, 566, A17
Yadav, V. K., Batham, S., Acharya, A. K., & Paul, R. 2014, in 2014 Int. Conf. Electronics and Communication Systems (ICECS) (Piscataway, NJ: IEEE), 1
Zavagno, A., Anderson, L. D., Russeil, D., et al. 2010a, A&A, 518 L101
Zavagno, A., Russeil, D., Motte, F., et al. 2010b, A&A, 518, L81
Zernickel, A., Schilke, P., & Smith, R. J. 2013, A&A, 554, L2
Zhang, Q., Qiu, K., Girart, J. M., et al. 2014, ApJ, 792, 116